

UCLA

UCLA Electronic Theses and Dissertations

Title

Microelectronic Sensors and Actuators Based on Novel Stiffness Variable Polymers

Permalink

<https://escholarship.org/uc/item/3mj183kb>

Author

Xie, Zhixin

Publication Date

2021

Peer reviewed|Thesis/dissertation

UNIVERSITY OF CALIFORNIA

Los Angeles

Microelectronic Sensors and Actuators
Based on Novel Stiffness Variable Polymers

A dissertation submitted in partial satisfaction of the
requirements for the degree Doctor of Philosophy
in Materials Science and Engineering

by

Zhixin Xie

2021

© Copyright by

Zhixin Xie

2021

ABSTRACT OF THE DISSERTATION

Microelectronic Sensors and Actuators
Based on Novel Stiffness Variable Polymers

by

Zhixin Xie

Doctor of Philosophy in Materials Science and Engineering

University of California, Los Angeles, 2021

Professor Qibing Pei, Chair

Materials with tunable stiffness responsive to stimuli are useful in a wide range of fields, such as soft robotics, reconfigurable structures and biomedical engineering. People have been pursuing stiffness variable materials for larger Young's modulus change and faster response rate. However, the broad transition temperature range of stiffness variable polymers means that excessive energy consumption is needed to heat and trigger the softening. And limited smart microelectronic devices were developed based on stiffness variable polymers.

We developed a series of stiffness variable polymers with narrow transition temperature range, high moduli change ratio. The transition temperature can be tuned to body temperature range,

which provides opportunities to build thermal-responsive, mechanically adaptive devices to be used on skin or in tissue. We also demonstrated the materials used as functional actuation materials.

In Chapter 1 and Chapter 2, we discussed the basics of stiffness variable materials. And we formulated a series of stiffness variable polymers with transition temperatures covering 30 °C to 43 °C, the Young's moduli of which can drop three to four orders of magnitude. The polymers' thermal and mechanical properties were characterized and discussed. Because the transition can be triggered by body temperature, they can be used for thermal-responsive, mechanically adaptive neural interfaces, which are rigid before implantation and become soft after implantation.

In Chapter 3, based on these polymers, the application as neural interfaces were explored. Intracortical probes were fabricated on the softening polymer showing great promise to provide tissue-like contact and reduce the micromotion around the tip. Based on the same polymer, we designed a multimodal neural probe that can simultaneously sense serotonin signal and electrophysiological signal. *In vitro* and *ex vivo* characterization of the neural probe were performed.

In Chapter 4, the softening polymer was used as a substrate to achieve a stretchable epidural electrode array for spinal cord. The silver nanowire and the wrinkled Parylene-C enabled the 20% stretchability for this device.

In Chapter 5, based on the stiffness variable polymer with transition temperature 43 °C, we designed and prototyped a Braille display. Carbon nanotubes were micropatterned as Joule heating electrode to trigger the softening of the polymer membrane, allowing for localized pneumatic actuation in the softened area.

These stiffness variable polymers with the transition temperature ranging from 30 °C to 43 °C demonstrated the promise to fabricate tissue-like electronics. These polymers can tolerate microfabrication process, and their sharp moduli change enabled a series of smart structures and devices to better adapt to the change of working conditions.

The dissertation of Zhixin Xie is approved.

Lihua Jin

Ximin He

Yu Huang

Qibing Pei, Committee Chair

University of California, Los Angeles

2021

Dedicated to my parents,

Kan Xie and Ying Li

for their unconditional love and support

Table of Contents

List of Figures.....	xii
List of Tables	xix
Acronyms	xx
Acknowledgements	xxii
Vitas.....	xxiv
Chapter 1. Introduction.....	1
1.1 Stiffness Variable Materials.....	1
1.2 Thermally Responsive Stiffness Variable Polymers.....	6
1.3 Current Challenges and Future Directions for Stiffness Variable Polymers	8
1.4 Motivation and Research Scope.....	9
Chapter 2. Body Temperature Triggered Stiffness Variable Polymers for Neural Interfaces	12
2.1 Introduction.....	12
2.2 Proposed Methods.....	15

2.3 Experiment section.....	16
2.3.1 Materials	16
2.3.2 Polymer Sample Preparation.....	17
2.3.3 Characterization Methods	17
2.3.4 Biocompatibility Test of Polymers	18
2.4 Results and Discussion	19
2.4.1 Effect of Side Chain Length	19
2.4.2 Effect of Crosslinker TMPTA	21
2.4.3 Effect of Acrylic Acid.....	24
2.4.4 Body Temperature Triggered Stiffness Variable Polymers for Bio Application	25
2.4.5 Biocompatibility Evaluation	32
2.5 Conclusion	34
Chapter 3. Thermal-responsive, Mechanically Adaptive Neural Probes	36
3.1 Introduction.....	36
3.2 Proposed Methods.....	38
3.3 Experiment Section.....	39

3.3.1 Materials	39
3.3.2 Fabrication of Intracortical Arrays on SP2	40
3.3.3 Fabrication of Multimodal Neural Probes on SP2.....	41
3.3.4 Preparation of Brain Phantom for <i>In Vitro</i> Study	42
3.3.5 Electrochemical Impedance Spectroscopy (EIS).....	42
3.3.6 Surgical Implantation of Intracortical Probe.....	43
3.3.7 <i>Ex vivo</i> Experiments for Serotonin Sensing.....	44
3.4 Results and Discussion	45
3.4.1 Insertion Buckling Assessment.....	46
3.4.2 Finite Element Analysis.....	47
3.4.3 <i>In vitro</i> Strain Field Characterization	49
3.4.4 Electrical Impedance Characterization <i>In Vitro</i>	52
3.4.5 <i>In Vivo</i> Electrophysiological Recording	53
3.4.6 Field-effect Transistor Based on the Thermal-responsive Polymer	56
3.4.7 <i>In Vitro</i> and <i>Ex Vivo</i> Serotonin Sensing	59
3.5 Conclusion	61

Chapter 4. Stretchable, Self-softening Epidural Electrode Array	62
4.1 Introduction.....	62
4.1.1 Epidural Electrode Arrays for Spinal Cord Stimulation.....	62
4.1.2 Stretchable Conductive Materials.....	63
4.2 Proposed Methods.....	65
4.3 Experiment Section.....	67
4.3.1 Materials	67
4.3.2 Fabrication of Epidural Electrode Array.....	67
4.4 Results and Discussion	70
4.5 Conclusion	75
 Chapter 5. A 2D Refreshable Braille Display Based on a Stiffness Variable Polymer and Pneumatic Actuation	 77
5.1 Introduction.....	77
5.2 Proposed Methods.....	79
5.3 Experiment Section.....	80
5.3.1 Materials	81

5.3.2 Stiffness Variable Polymers.....	81
5.3.3 Design of Joule Heating Electrode	82
5.3.4 Fabrication Process	83
5.4 Results and Discussion	86
5.5 Conclusion	89
Chapter 6. Conclusion and Future Remarks	90
6.1 Conclusion	90
6.2 Outlook and Future Works.....	92
Reference	95

List of Figures

Figure 1.1 Pictures of a sea cucumber in relaxed (left) and stiffened (right) state showing the variable stiffness in response to the external stimuli (Photos citation:[2])..... 2

Figure 1.2 Dielectric elastomer grippers with variable stiffness by embedded low melting point alloys in silicone substrate (photo citation:[7])..... 3

Figure 1.3 Photos showing a stiffness variable catheter changing its curvature by external magnetic field (Photo citation:[9])..... 4

Figure 1.4 Modulus change ratio of representative stiffness variable materials..... 5

Figure 1.5 Molecular structure of stearyl acrylate and UDA (left). Moduli vs. temperature for the stiffness variable polymers (right, figure adapted from Ref. 21)..... 7

Figure 2.1 Mechanical mismatch between common implanted materials and nerve tissues..... 13

Figure 2.2 Molecular structures of several key components investigated for the stiffness variable polymers..... 16

Figure 2.3 Modulus vs. temperature for polymers with different crystallizable side chains. 20

Figure 2.4 (a) Modulus vs. temperature and **(b)** Stress-strain curve of the polymers with different TMPTA percentage..... 22

Figure 2.5 (a) Modulus vs. temperature and (b) Stress-strain curve of the polymers with different AA percentage.	24
Figure 2.6 (a) Modulus vs. temperature and (b) Stress-strain curves of the polymers SP1 to SP4 with different transition temperature.	28
Figure 2.7 Wide angle X-ray diffraction of the softening polymers with the crystalline domain	29
Figure 2.8 DSC of the four softening polymers showing the phase transition properties of the polymers.....	29
Figure 2.9 Swelling rate of softening polymers in phosphate-buffered saline at 37 °C.	30
Figure 2.10 Photos of the polymer SP2 softening on a rat brain.	31
Figure 2.11 Comparison of Young’s moduli and softening response time between previously reported materials and softening polymers developed in this work (bottom, red).	31
Figure 2.12 Microscopic image of labeling of neuroepithelial cell NE-4C after 24 hours coculturing with softening polymers.	33
Figure 2.13 Evaluation of neuroepithelial cell NE-4C’s survival in response to the polymer (SP1, SP2, SP3, and SP4) and control materials.	34
Figure 3.1 Mechanisms of sensing neurotransmitters based on the FET-Aptamer sensor reported before in Ref [71]......	37

Figure 3.2 Fabrication process flow of building neural probes on the body temperature triggered softening polymer substrate SP2.....	39
Figure 3.3 Scanning electron microscope image of the intracortical probe (left) and the optical microscope image of the conductive electrode traces (right)	45
Figure 3.4 (a) Maximum force before buckling of different thickness of SP2 strips and buckling rate of insertion into 0.6% agarose tissue phantom (n=15 for each thickness). (b) Photos of the penetration of the softening polymer probe into rat brain.	46
Figure 3.5 (a) 3D quarter-symmetric finite element model with a shank probe (orange) inserted into brain tissue (blue). Strain profiles induced in the brain tissue by 20 μ m displacement with (b) polyimide probe and (c) the softening polymer.....	48
Figure 3.6 <i>In vitro</i> strain field characterization. (a) Bright field images of a dummy polyimide probe and softening polymer SP2 probe inserted into the agarose tissue phantom. (b) Strain field plots after a 20-micron axial displacement was applied to devices to mimic micromotion from accelerations.....	50
Figure 3.7 Average profiles of the displacement magnitude as a function of distance from the device for polyimide and softening polymer SP2.....	51
Figure 3.8 Impedance map after bending cycle tests with 0.5 mm bending radius at different frequencies.	52

Figure 3.9 Impedance map of the fabricated intracortical probe after soaking in PBS for 19 days. 53

Figure 3.10 Schematic illustration of the *in vivo* experiment using softening polymer based intracortical array for neural activity recording. 54

Figure 3.11 Recorded signal of repetitive firing shows amplitude accommodation typical of excitatory neurons. 54

Figure 3.12 Electrophysiology recording of cortical response with respect to leg muscle movements in response to spinal cord stimulation. 55

Figure 3.13 (a) Cross-sectional structure of the multimodal neural probe. **(b)** Optical microscopy image of the fabricated softening polymer based multimodal neural probe where two electrophysiological electrodes are on the top and an In₂O₃ nanoribbon field-effect transistor (FET) is on the bottom (Scale bar: 200 μm). **(c)** Serotonin sensing mechanism: Conformation change after serotonin capture leads to the change of transconductance of In₂O₃. 57

Figure 3.14 (a) Representative transfer characteristics of the In₂O₃ FETs in liquid gating configuration of aCSF. Left: source-drain current ($I_{DS}-V_{GS}$), right: source-gate current ($I_{GS}-V_{GS}$). The source-drain voltage V_{DS} was at constant of 500 mV. **(b)** Representative output characteristics of the In₂O₃ FETs in aCSF. 58

Figure 3.15 (a) Representative serotonin response curves in aCSF, where concentration-dependent increases were observed in source-drain currents while sweeping V_{GS} . **(b)** Calibrated responses of serotonin in aCSF from 10 fM to 100 μM. N = 3. Error bars: standard error means. 59

Figure 3.16 (a) Schematics of serotonin aptamer field-effect transistor (FET) biosensors *ex vivo* characterization in brain tissue. **(b)** Representative transfer characteristics of the In₂O₃ FET (green curve) and the gate-source voltage V_{GS} (orange curve). **(c)** Concentration-dependent responses for serotonin-aptamer functionalized FETs in homogenized brain tissue..... 60

Figure 4.1 Electronic dura mater fabricated on PDMS using microcracked gold for stretchable neural interfaces (Photo citation [45]). 63

Figure 4.2 Chronic softening spinal cord stimulator with serpentine patterned electrodes (Photo citation: [94]). 64

Figure 4.3 (a) SEM image of the silver nanowires. **(b)** Chemical structure of the (hydroxypropyl)methyl cellulose. **(c)** Conductivity change of screen-printed AgNW/PUA composite conductors as a function of tensile strain with various line widths (Photo citation: [97]). 65

Figure 4.4 Schematic illustration of the stretchable epidural array based on silver nanowires and wrinkled Parylene-C. 66

Figure 4.5 Geometry of the designed epidural electrode array..... 66

Figure 4.6 Fabrication process of the stretchable electrode array on softening polymer SP2. 69

Figure 4.7 Microscopic image of a representative serpentine pattern with the AgNW ink..... 70

Figure 4.8 Image of the fabricated stretchable epidural electrode array with wrinkled Parylene-C encapsulation.....	71
Figure 4.9 Microscopic image of the wrinkled Parylene-C in non-patterned area.	72
Figure 4.10 Electrical impedance measured in PBS before and after a uniaxial strain of 20%. .	72
Figure 4.11 Relative resistance change of the silver nanowire conductive traces after cyclic 20% stretching (n=8).....	74
Figure 4.12 Impedance change of the stretchable, self-softening electrode array after cyclic 20% stretching (n=8).....	75
Figure 5.1 Representative actuators used in Braille displays. (a) Piezoelectric unimorph actuators used in P16 Braille cells (metec AG, Germany). (b) Electromagnetic actuators for Braille display (picture citation [99]). (c) Pneumatic actuators for Braille display (picture citation [100]).....	77
Figure 5.2 (a) Schematic illustration of the structure of the Braille PolyPad and (b) the cross-sectional working principle.....	80
Figure 5.3 (a) Storage modulus and $\tan \delta$ versus temperature profile of the BSEP. (b) Stress strain curve of the BSEP membrane.	82
Figure 5.4 (a) Design of the serpentine carbon nanotube (CNT) electrode for localized Joule heating. (b) Design and dimension of the PCB top side for Joule heating control (Yellow: copper contact. Gray: Air channel). (c) Top view of the PCB.	83

Figure 5.5 Fabrication process of the CNT pattern BSEP membrane. 84

Figure 5.6 Image of CNT electrodes transferred onto the stiffness variable polymer membrane followed by lamination on to PCB..... 85

Figure 5.7 (a) Blocking force required to completely press down an actuated BSEP membranes of specified thickness. **(b)** Photo image and IR images of a dot before and during actuation. **(c)** Joule heating temperature ramp with different heating voltage. **(d)** IR image of a cell during Joule heating at specified voltages. 86

Figure 5.8 (a) IR image of one line Braille cells being Joule heated at 30 V. All dots are heated above the 45 °C transition temperature within 0.5 s. The power consumption at this voltage for heating 60 dots was estimated to be ~0.6 W. **(b)** The actuation of one line Braille cells of the PolyPad. 88

List of Tables

Table 1 Formulations of prepolymer solutions for side chain length study.....	19
Table 2 Formulations of prepolymer solutions for TMPTA study	22
Table 3 Formulations of prepolymer solutions for AA study	24
Table 4 Formulations of prepolymer solutions for various softening polymer.....	26
Table 5 Transition temperatures and moduli of the softening polymers.....	27
Table 6 Summary of FEA parameters.....	48
Table 7 Formula of stiffness variable polymer membrane	81

Acronyms

AA	Acrylic acid
aCSF	Artificial cerebrospinal fluid
AgNWs	Silver nanowires
BSEP	Bistable electroactive polymer
CNT	Carbon nanotube
DSC	Differential scanning calorimetry
DMA	Dynamic mechanical analysis
DMPA	2,2-Dimethoxy-2-phenylacetophenone
EIS	Electrochemical Impedance Spectroscopy
EMG	Electromyography
FEA	Finite Element Analysis
FET	Field-effect transistor
HA	Hexadecyl acrylate
PBS	Phosphate-buffered saline

PCB	Printed circuit board
PDMS	Polydimethylsiloxane
SA	Stearyl acrylate
SP	Softening polymer
TA	Tetradecyl acrylate
TMPTA	Trimethylolpropane triacrylate
UDA	Urethane diacrylate
XRD	X-ray diffraction

Acknowledgements

As I am close to the end of the Ph.D. journey, I start to cherish every second that I am still a UCLA student. These years in UCLA has taught me devotion, collaboration and perseverance. I am so grateful that I came to UCLA and met so many amazing people around me.

First and foremost, I would like to express my sincere appreciation for my advisor, Professor Qibing Pei. As my advisor, he has shown me, by his example, what a good scientist and person should be. Without his continued guidance and support, the completion of this dissertation would not be possible.

I am deeply grateful to Professor Lihua Jin, Professor Ximin He and Professor Yu Huang for serving as members of the committee. Their expertise in the materials science field and advice in my research were so precious and important. I also really appreciate them for letting my defense be an enjoyable moment.

I would like to express my sincere gratitude to my project collaborators, Professor Reggie Edgerton, Professor Anne Andrews, Dr. Chuanzhen Zhao, Dr. Parag Gad, Dr. Hui Zhong. I enjoyed every discussion that we had. Without your support and dedication to the project, the collaboration would not be done.

My group members from Professor Qibing Pei's group, Dr. Rujun Ma, Dr. Xiaofeng Liu, Dr. Zhi Ren, Dr. Wei Hu, Dr. Chao Liu, Dr. Yuan Meng, Dr. Ye Shi, Dr. Huier Gao, Dr. Shu-Yu Chou, Dr. Ziyang Zhang, Dr. Yayun Liu, Dr. Meng Gao, Hanxiang Wu, Jinsung Kim, Zihang Peng,

Juhong Pu, all deserve my most sincere gratitude for their generous support. I will most certainly miss the days we worked together in the soft materials research lab.

Chapter 2 and Chapter 3 is written based on Xie, Z., Zhao, C., Wu, H., Gad, P., Zhong, H., Liu W., Hu J., Meng Y., Li Z., Wu, L., Weiss P., Edgerton R., Andrews A., Pei Q. “Mechanically Adaptive Polymer For Tissue-like Multimodal Neural Interfaces.” Manuscript in preparation.

Chapter 5 is reprinted with permission from Xie, Z., Kim, J., Peng Z., Qiu, Y. and Pei, Q. “A 2D Refreshable Braille Display Based on a Stiffness Variable Polymer and Pneumatic Actuation.” *Electroactive Polymer Actuators and Devices (EAPAD) XXIII*. Vol. 11587. International Society for Optics and Photonics, 2021. DOI: 10.1117/12.2584039

To my best friends in Los Angeles, Zhou Li, Yekan Wang, Yao Yang, Yepin Zhao, Zirui Liu. Without you, my life in Los Angeles would not be the same. I know you are always by my side every time I am down. Thank you and our friendship will stand the test of time.

My beloved girlfriend Yan Ding, who has been supporting me, encouraging me and inspiring me in the past four years despite the long distance. Thank you for your patience and perseverance through the hard time. Thank you for supporting me in pursuit of my career goal. Without your understanding, this dissertation would not be possible. I owe you too much companionship and love.

Lastly, I cannot thank my family enough, especially my father Kan Xie and my mother Ying Li, who have been giving me unconditional love and support. Thank you for giving me strength and courage to reach for stars and chase my dream. I could not have done this without you.

Vitas

2015 B.S., Polymer Materials and Engineering, Zhejiang University, Hangzhou, China

2015-2021 Ph.D. Student at Department of Material Science & Engineering, University of California at Los Angeles, CA, USA

2019 Intern, Advanced Technology Department, Lam Research, Fremont, CA

2020 Intern, Panel Process & Optics, Apple, Inc., Cupertino, CA

Publications

Zhixin Xie, Jinsung Kim, Zihang Peng, Yu Qiu and Qibing Pei. “A 2D Refreshable Braille Display Based on a Stiffness Variable Polymer and Pneumatic Actuation.” *Electroactive Polymer Actuators and Devices (EAPAD) XXIII*. Vol. 11587. International Society for Optics and Photonics, 2021. DOI: 10.1117/12.2584039

Zhixin Xie, Chuanzhen Zhao, Hanxiang Wu, Parag Gad, Hui Zhong, Wenfei Liu, Junhui Hu, Yuan Meng, Zhou Li, Lily Wu, Paul S. Weiss, V. Reggie Edgerton, Anne M. Andrews and Qibing Pei. “Mechanically Adaptive Polymer For Tissue-like Multimodal Neural Interfaces.” Manuscript in preparation.

Zhixin Xie, Hexing Yin, Jinsung Kim, Parag Gad, Hui Zhong, V. Reggie Edgerton and Qibing Pei. “Stretchable, self-softening epidural electrode array.” Manuscript in preparation.

Zihang Peng, Ye Shi, **Zhixin Xie**, Yanji Li, Norris Chen, Qibing Pei. "Self-clearable Bilayer Electrode for Dielectric Elastomer Actuators." *SPIE Electroactive Polymer Actuators and Devices (EAPAD) XXIII*. Accepted.

Meng Gao, Hanxiang Wu, Roshan Plamthottam, **Zhixin Xie**, Ying Liu, Junhui Hu, Shuwang Wu, Lily Wu, Ximin He and Qibing Pei. "Skin Temperature Triggered, Debonding-on-Demand Sticker for a Self-Powered Mechanosensitive Communication System." *Matter (2021)*. Accepted.

Junhong Pu, Yuan Meng, Zihang Peng, Jianghan Wu, **Zhixin Xie** and Qibing Pei. "A dielectric elastomer comprising electrophoretically concentrated boron nitride nanosheets for large out-of-plane actuation". Manuscript in preparation.

Abubekkerov, Mark, Junnian Wei, Kevin R. Swartz, **Zhixin Xie**, Qibing Pei, and Paula L. Diaconescu. "Preparation of multiblock copolymers via step-wise addition of l-lactide and trimethylene carbonate." *Chemical Science* 9, no. 8 (2018): 2168-2178.

Zhang, Ziyang, Adie Alwen, Hongming Lyu, Xiangyu Liu, Zhou Li, **Zhixin Xie**, Yu Xie, Fangyi Guan, Aydin Babakhani, and Qibing Pei. "Stretchable Transparent Wireless Charging Coil Fabricated by Negative Transfer Printing." *ACS Applied materials & Interfaces* 11, no. 43 (2019): 40677-40684.

Hu, Wei, Zhi Ren, Junpeng Li, Erin Askounis, **Zhixin Xie**, and Qibing Pei. "New dielectric elastomers with variable moduli." *Advanced Functional Materials* 25, no. 30 (2015): 4827-4836.

Chapter 1. Introduction

1.1 Stiffness Variable Materials

The stiffness of a material is the property to resist deformation. Common engineering materials have constant stiffness over the operational conditions, so that they can meet the force loading and outputs requirements.

In some cases where the environments are changing, the mechanical loads requirements may vary.^[1] For example, when robotic grippers grasping an egg and then a cup of water, the required force output is quite different. To better accommodate this change, people are pursuing materials with tunable stiffness responsive to external stimuli.

Nature has provided a good example of stiffness variable material: the sea cucumber (**Fig. 1.1**). The dermis of the sea cucumber contains nano-sized collagen fibrils that can interact with each other to form a rigid structure. With the modulation of released biomolecules, the fibrils will decouple to switch to the soft state. This reversible interaction mechanism has inspired a lot of man-made stiffness variable materials.



Figure 1.1 Pictures of a sea cucumber in relaxed (left) and stiffened (right) state showing the variable stiffness in response to the external stimuli (Photos citation:[2]).

These stiffness variable materials are useful in a wide range of fields. In robotics, the adjustable stiffness gripper can provide stable configurations, different output force and controllable interaction modes with the environments.^[3] **Fig 1.2** is an example of variable stiffness grippers composed of dielectric elastomer actuators (DEA) and a low-melting-point alloy embedded in silicone. The grippers can bend in response to the electrical field at the soft state and can be stiffened for high force output in the rigid state. In other applications, stiffness variable materials can also ensure the safety interaction between robots and human.^[4]

Another example application is in morphing structures, people have been pursuing the morphing wings for aircrafts^[5] so as to enhance the aerodynamic performance. Stiffness variable materials can permit structural components to undergo large-scale, in-service changes in geometry.^[6] The effective modulus range, and the specific effective modulus need to be considered for structural materials.

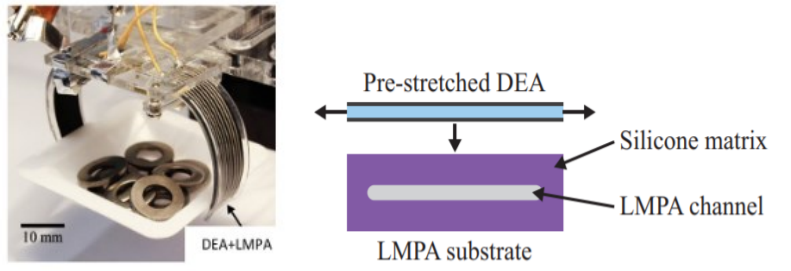


Figure 1.2 Dielectric elastomer grippers with variable stiffness by embedded low melting point alloys in silicone substrate (photo citation:[7]).

In biomedical devices, smart prosthetics have been developed to modulate the stiffness of joint.^[8] Catheters with variable stiffness can offer dexterity to navigate in the complex environments inside human body (**Fig. 1.3**).^[9] Manipulators with tunable stiffness can control the interactions with tissues in minimally invasive surgeries.^[10] More applications include endoscopes and neural probes that can adapt to the stiffness of soft tissue. Therefore, people have been interested in developing and optimizing materials with tunable stiffness to enable more smart structures and tools.

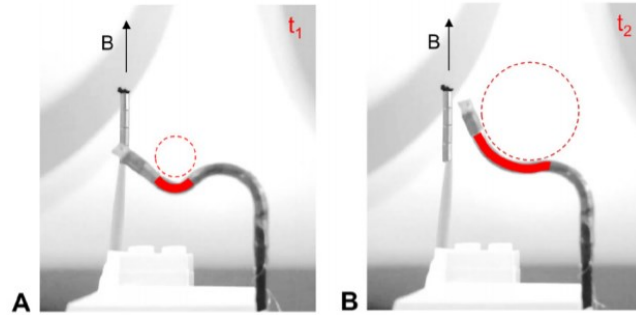


Figure 1.3 Photos showing a stiffness variable catheter changing its curvature by external magnetic field (Photo citation:[9]).

Different mechanisms have been brought up to develop stiffness variable materials, such as electrorheological fluids, thermoplastics, low melting point alloys, etc. These mechanisms can be divided into two main categories. One is by insertion and subtraction of soft media (gas or solvent), for example, pneumatic stiffness variable actuators. But this requires the reliable encapsulation of the mobile medium. Another is by microstructure change or phase change, for example, shape memory polymers and shape memory alloys. These microstructure transformations will induce Young's modulus change of the material, thus change the stiffness. Young's modulus is the relative stiffness of a material, which is measured by the slope of elastic zone of a stress and strain curve. Stainless steel has Young's modulus around 200 GPa, while silicone rubber has Young's

modulus of several MPa. **Fig. 1.4** summarizes several representative stiffness variable materials, and their moduli change ratio.

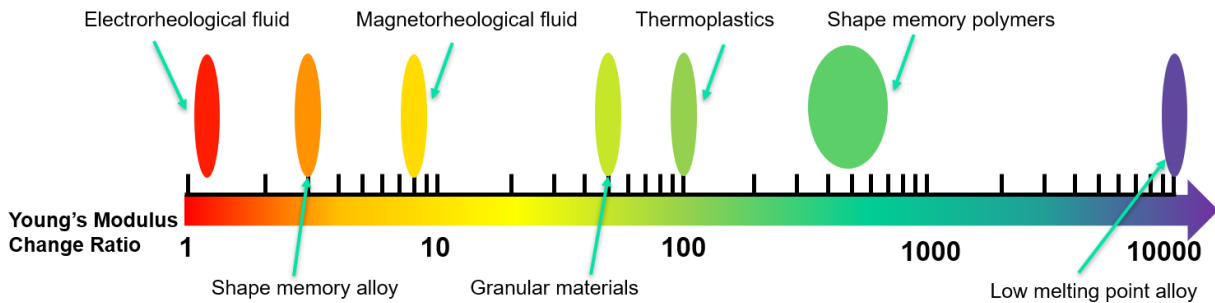


Figure 1.4 Modulus change ratio of representative stiffness variable materials.

As is shown, electrorheological fluid and magnetorheological fluid are materials with variable stiffness triggered by external field. This category of materials also includes the fluid-polymer composites. The modulus change ratio is usually below $10\times$. Low melting point alloys, such as Gallium Indium eutectic, have modulus change over $10000\times$. But handling this liquid metal above transition temperature requires fully encapsulation of it, thus increases the processing complexity. Common thermoplastics can undergo the glass transition upon heating, thus result in a modulus change $5\text{--}100\times$. Above the glass transition temperature (T_g), polymer chain segments become more mobile, which lead to the rubber-like behavior. In particular, thermoplastic shape memory polymers, as a subset of thermoplastics, have raised particular interest for variable rigidity over hundreds of times responsive to temperature. Compared with stiffness variable composite materials, such as granular materials or fluid-polymer composites, shape memory polymers, as a monolithic material, are easier to be processed for electronics devices including stiffness variable actuators and sensors.^[11]

1.2 Thermally Responsive Stiffness Variable Polymers

Compared with other stiffness variable materials like shape memory alloys, polymers are lightweight, easily processable and can be chemically tailored in the molecular structure to tune the moduli change and overall properties. Although stiffness variable polymer responsive to UV^[12] or water^[13] has been studied and developed, thermally responsive stiffness variable polymers that can be softened by heat still remain the a favorable way to achieve large stiffness change.

In thermally active stiffness variable polymers, modulus change is induced by heating the polymer through a transition, such as glass transition, or as crystalline melting, leading to a considerable drop in modulus.^[14] The glass transition of amorphous polymers usually occurs in a wide temperature span (10 °C~30 °C), leading to Young's moduli changes of up to 3 orders of magnitude.^[15, 16] Sometimes, this thermal transition can be enhanced by effect of water-assisted plasticization of the polymer.^[17] As an example, Ware et. al^[18] synthesized a thermally responsive and water sensitive stiffness variable polymer based on commercially-available acrylate monomers. The water uptake leads to the thermal-activated modulus change at a lower temperature. Therefore, the modulus of the polymer can drop three orders of magnitude in body fluid at 37 °C. But the softening process takes at least 24 hours to finish.

Incorporating crystalline domain into the polymer network, the Young's modulus can also be tuned by controlling the temperature above or below the melting point of the crystalized segments. For example, poly(caprolactone)s (PCLs), poly(lactide)s (PLAs), poly(ω -pentadecalactone)s are often considered as building blocks for stiffness variable or shape memory polymers. The typical melting points of which are 60 to 75 °C.^[19] These polymers form semi-crystalline domain because

of the crystallizable backbones. On the other hand, the crystallizable side chains can also be used to control the crystallinity and the stiffness. A well-defined bottlebrush polymer^[20] with wax-like crystalline sidechains has been synthesized precisely as a reversibly moldable polymer with tunable stiffness.

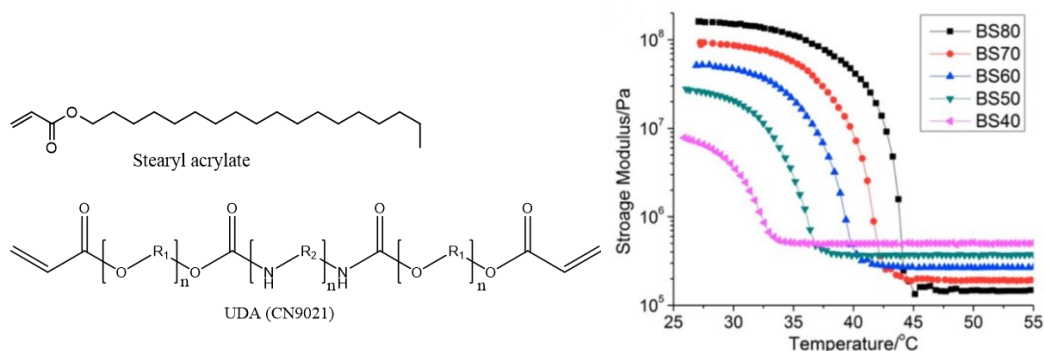


Figure 1.5 Molecular structure of stearyl acrylate and UDA (left). Moduli vs. temperature for the stiffness variable polymers (right, figure adapted from Ref. 21).

In 2016, our group also developed a bistable electroactive polymer^[21] as a stiffness variable electroactive material based on crystalline side chains. The polymers mainly consist of stearyl acrylate (SA) and urethane diacrylate (UDA) macro-crosslinker. The long alkyl chain of SA can form nanocrystalline domain below transition temperature, and to fix the deformation after actuation. As shown in **Fig. 1.5** right, the largest modulus change came from the polymer “BS80” with three orders of magnitude modulus drop at 43 °C. Decreasing the SA percentage in the polymer system lowers the transition temperature, but the modulus change ratio was also sacrificed.

This bistable phase change polymers based on SA show great potential to be used as stiffness variable polymers, because the thermal activated phase transition leads to larger modulus drop compared with other shape memory polymers. And the formulation and free radical polymerization of the polymer system is straightforward without complicated organic synthesis steps.

1.3 Current Challenges and Future Directions for Stiffness Variable Polymers

Despite the great progress in stiffness variable polymers, fundamental developments are still required to further improve these materials.

First challenge is how to widen the range of available stiffness. Currently, the stiffness variable polymers have relatively lower Young's modulus, in the rigid state, compared with alloys. But for morphing structures applications, the materials need to have high rigidity as well as toughness to meet the loading requirements for structural materials. In the soft state, due to the intrinsic self-entanglements of the polymer chains, common elastomers cannot go below 100 kPa range. In some biomedical applications where supersoft materials are desired to match the stiffness of soft tissue, the stiffness variable polymers need to be further improved to reach kPa in Young's modulus.

Second challenge is to increase the modulus change ratio and precisely control the modulus. Common shape memory polymers can change Young's modulus ~ 3 orders of magnitude. There is still room to further enlarge the stiffness change. On the other hand, stiffness variable polymers are usually used in two modes, i.e., the stiff state and the soft state. Precisely getting a target

modulus in the middle can be difficult. A material of which the modulus can be linearly tuned can be very useful.

Thirdly, reversibility of modulus change can be improved. Phase change polymers usually take longer time to be stiffened than softened. Sometimes, the insufficient time can lead to decayed recovery of stiffness. For materials that undergo cyclic changes, the improvement of reversibility deserves further investigations.

Lastly, more external stimuli can be combined into stiffness variable polymers to create different functional devices, such as stiffness variable dielectric actuators.^[22] Pressure, temperature, light, electrical signal, glucose, biomolecules can all be coupled into the devices to enhance or utilize the stiffness variation effect.

1.4 Motivation and Research Scope

The stiffness variable polymer BS80 that our group developed^[21] based on SA has tunable stiffness from 0.16 GPa to 0.2MPa, with the transition temperature ~ 43 °C. The stiffness change occurs in a relatively broad temperature range ~ 7 °C. And heating is needed to trigger the stiffness change, which also means embedded heating circuits as well as energy consumption. Therefore, starting from this phase changing polymer, if we could lower the transition temperature to body temperature range to get a very sharp modulus drop, a self-softening material (without external heating circuits) can be realized and used in biomedical applications. Meanwhile, using our stiffness variable polymers as the substrates, a variety of microelectronic sensors and actuators can be fabricated to achieve different types of thermal-responsive, smart devices.

The first part of the dissertation will focus on how we developed a series of novel stiffness polymers with the transition temperature ranging from 32 °C to 43 °C, covering the body temperature range. The effects of crystallizable side chains, small molecule crosslinker and acrylic acid (AA) were investigated. As a result, the modulus change ratio was increased to 4 orders of magnitude within a narrow temperature window, and the polymers can reach kPa range softness. These features provide opportunities to build thermal-responsive, mechanically adaptive devices to be used on skin or in tissue.

The second part of the dissertation will focus on how sensors and actuators were built on the stiffness variable polymer substrate to achieve different functions. For example, neural probes were fabricated based on the softening polymer that can adapt to the softness of neural tissue after implantation. A Braille display using stiffness variable polymer to selectively control the actuation was also demonstrated.

Based on the work completed during my Ph.D. study, this dissertation is divided into six chapters: Chapter 1, the current chapter, provides a brief introduction of the stiffness materials and stiffness variable polymers, including current challenges and future directions to improve these materials.

Chapter 2 presents the development of a series of body temperature triggered stiffness variable polymers. The effects of several key components in the prepolymer solution were investigated, including the side chain length, the small molecule crosslinker, and the acrylic acid. The polymers' thermal, mechanical properties and biocompatibility were characterized and discussed. Because the transition can be triggered by body temperature, they can be used for thermal-responsive,

mechanically adaptive neural interfaces, which are rigid before implantation and become soft after implantation.

Chapter 3 described the development of thermal-responsive, mechanically adaptive neural probes with the polymer substrates. First, an intracortical probe was designed and fabricated with the softening polymer substrate. The microfabricated probe on the mechanically adaptive polymer shows great promise to provide tissue-like contact with soft neural tissue and reduce the micromotion around the tip. Then, based on the same polymer substrate, we designed a multimodal neural probe that can simultaneously sense serotonin signal and electrophysiological signal. The working mechanism for serotonin sensing is an aptamer-based field-effect transistor (FET). *In vitro* and *ex vivo* sensing of the serotonin sensor were demonstrated.

Chapter 4 demonstrated a stretchable epidural array for spinal cord use based on the softening polymer substrate. The silver nanowire and the self-formed wrinkled Parylene-C enabled the 20% stretchability for the device. The electrical property remains stable after stretching cycles, showing the potential of the polymer-based electrode as a versatile platform technology to create different tools for biomedical study.

Chapter 5 introduced a Braille display based on the stiffness variable polymer with transition temperature 43 °C. Carbon nanotubes were patterned on the polymer to trigger the softening of the stiffness variable polymer membrane, allowing for localized pneumatic actuation in the softened pin area.

Chapter 6 summarized the dissertation. The outlook for future research in stiffness variable polymers and devices was discussed.

Chapter 2. Body Temperature Triggered Stiffness

Variable Polymers for Neural Interfaces

2.1 Introduction

Bidirectional interfacing with the nervous system enables neuroscience research, diagnosis, and therapies.^[23-25] This two-way communication allows us to monitor the neural signal or modulate the neural process to understand diseases and restore functions.

Compared with non-invasive approaches (*e.g.*, scalp electroencephalography), the invasive neural interfaces such as intracortical electrode arrays and epidural electrode arrays have enabled signal recording and neural modulation with higher spatiotemporal resolution^[26-29] and a more specific, accurate communication. However, most of the state-of-the-art devices are fabricated on silicon substrate using conventional microfabrication techniques^[30], which have huge mechanical mismatch between the rigid silicon substrate and the soft neural tissue. Silicon has Young's modulus ~ 170 GPa^[31, 32] while the central nervous system (CNS) tissues have Young's moduli between 100 Pa and 10 kPa (**Fig. 2.1**).^[33] The mechanical mismatch induces immunological responses due to the micromotion between neural tissue and the device,^[34, 35] leading to glial activation and unfavorable effects on nearby neurons and formation of nonconductive fibrotic scar.^[36, 37] Recent studies have shown that microelectronics with reduced mechanical stiffness close to nerve tissues introduced less inflammatory responses and provided intimate and stable

electrical pathways.^[38-40] Therefore, it is important to develop implantable neural devices with decreased stiffnesses close to tissues.

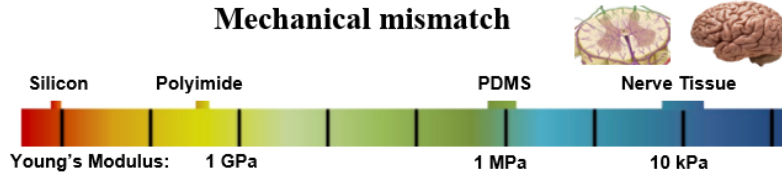


Figure 2.1 Mechanical mismatch between common implanted materials and nerve tissues

One strategy for developing imperceptible, tissue-like neural interfaces is to fabricate ultrathin polymer electronics (thickness $<1 \mu\text{m}$) using polyimide or SU-8 substrates.^[32, 41-43] An alternative approach is to develop neural interfaces with soft polymers such as polydimethylsiloxane (PDMS, $\sim 1 \text{ MPa}$)^[44, 45] or hydrogels ^[46-48] ($\sim 30 \text{ kPa}$) that offer intimate and tissue-mimicking contacts. However, devices fabricated by both methods are difficult to be inserted into tissue during surgical implantation directly due to the low stiffness.^[49] For intracortical, deep brain, and intraspinal cord applications, it is necessary to adopt a rigid insertion shuttle^[42] or sacrificial stiff coatings^[50, 51] for neural tissue penetration without buckling, which includes complicated microfabrication process and may create extra tissue damage.^[52] Therefore, an ideal polymer substrate for implantable neural interfaces should be rigid during insertion and soft as an elastomer after implantation. Stiffness variable polymers are such materials providing the adaption to the change of requirements.

A few works have been done on smart adaptive polymers that can reduce stiffness under physiological environment. Capadona et. al^[2] developed a nanocomposite which has a large modulus change from 4200 MPa to 1.6 MPa after swelling in water. The cellulose whisker in this material can assemble into a percolating network upon evaporation of water. The interactions between cellulose whisker are switched off by the introduction of a chemical regulator that allows for competitive hydrogen bonding. Intracortical microelectrodes and implants have been developed based on this nanocomposite.^[53, 54] But the swelling of the polymer limits the geometry stability for long term applications.

Voit et. al^[18] built a thermally responsive and water sensitive shape memory polymer based on commercially available acrylate monomers. The devices which are stiff enough (shear modulus of ~700 MPa) to assist with device implantation and soft in body (~300 kPa), are capable of recording neural activity. But the softening process takes at least 24 hours to finish. The same group developed another thiol-ene/acrylate system^[55] which can soften from more than 1 GPa to 18 MPa on exposure to physiological conditions: reaching body temperature and taking up less than 3% fluid. In this work, it takes a week for the substrate to soften. Moreover, these polymers still have Young's moduli several orders of magnitude higher than nerve tissue.

Therefore, it is interesting to develop modulus adaptive polymers that has rapid transition rate and low water uptake to achieve tissue softness after implantation. Typically, thermally active shape memory polymers that have stiffness change in response to temperature requires external heating to trigger the transition. But implant biomedical applications require that the triggering temperature should be near the human body temperature (37 °C) to avoid tissue damage. Several strategies

have been attempted to tailor the shape-memory trigger temperature. For example, the melting point of polymers has been reduced by introducing low molar mass crystallizable ϵ -caprolactone^[19, 56] and by manipulating the size of phase-segregated hard segment domains.^[57]

2.2 Proposed Methods

We plan to modify the bistable phase change polymers (BS80)^[21] which are based on the crystallizable side chains, to tune the transition temperature and mechanical properties in order to get larger stiffness variation within body temperature range for neural interfaces.

Starting from the old recipe of BS80, stearyl acrylate (SA) was the main component for the crystalline domain formation. Urethane diacrylate (UDA) CN9021 is made of a flexible polyether diol segment and a relatively flexible aliphatic diisocyanate, which served as a macro-crosslinker to enhance the stretchability and toughness. Trimethylolpropane triacrylate (TMPTA), a trifunctional small molecule crosslinker was incorporated for increasing the crosslinking density and preventing chain slippage. 2,2-Dimethoxy-2-phenylacetophenone (DMPA) served as the photo initiator.

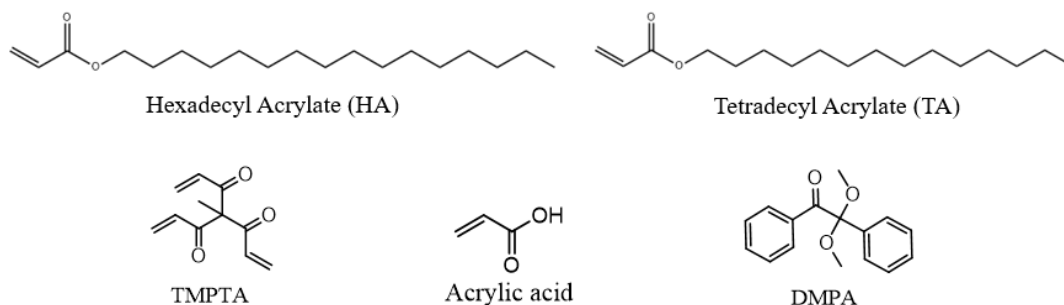


Figure 2.2 Molecular structures of several key components investigated for the stiffness variable polymers.

SA has 18 carbons in the alkyl chain, and the monomer has melting point of 32 °C. In comparison, among the homologous series of SA, hexadecyl acrylate (HA) has 16 carbons in the alkyl chain and tetradecyl acrylate (TA) has 14 carbons. The melting points of HA and TA monomer are 24 °C, 14 °C respectively. Therefore, by replacing SA with HA and TA, it is possible to lower the transition temperature of this polymer system.

Meanwhile, we also investigated the effect of TMPTA and acrylic acid in the polymer system, to understand the fundamental relationship between structure and thermomechanical properties.

2.3 Experiment section

2.3.1 Materials

Urethane diacrylate CN9021 was generously provided by Sartomer Company (Exton, PA). Hexadecyl acrylate (HA), tetradecyl acrylate (TA) were purchased from TCI America (Portland,

OR). Stearyl acrylate, trimethylolpropane triacrylate, acrylic acid and 2,2-Dimethoxy-2-phenylacetophenone were purchased from Sigma-Aldrich (St. Louis, MO). All chemicals were used as received without further purification.

2.3.2 Polymer Sample Preparation

Prepolymer solution was mixed according to the ingredients at specified ratios in **Table.1** at 60 °C. The heated solution was injected into a pair of glass slides separated by 90µm spacer. The sample was then cured by UV exposure using Dymax UV curing conveyor with a Fusion 300S type “H” UV curing bulb in ambient environment for 2min.

2.3.3 Characterization Methods

Mechanical properties were measured on a TA Instruments RSAIII dynamic mechanical analyzer (DMA). Dynamic temperature sweep tests were conducted at a temperature ramping rate of 2 °C/min and a frequency of 1 Hz from 20 to 48 °C with samples of 6 mm wide and ~0.09 mm thick. The stress–strain curves of the rubbery copolymers were obtained at 45 °C at a stretching rate of 0.5/s. The tested samples used were 6 mm wide and ~90 µm thick.

Differential scanning calorimetry (DSC) of the softening polymers was carried out on PerkinElmer Instruments, Pyris Diamond DSC. Polymer samples were cut into small debris and weighted ~3 mg. The crucibles are first cooled to 5 °C, then heating to 40 °C at a heating/cooling rate of 5 °C/min.

Wide-angle X-ray diffraction measurements (XRD) tests were performed on Bruker D8 Discover X-ray Diffractometer with thin film samples (90 μm thick) using Cu K α radiation with a 2θ step size of 0.05° .

Swelling ratio was measured by weight change after immersion in phosphate-buffered saline (PBS) at 37°C at several time points for 4 weeks. Samples are cut into 2 cm \times 1 cm strips. The dry mass of each sample was measured and recorded with a balance with 0.01 mg precision. At each desired time point, each sample was removed from the PBS, and the surface of the polymer was gently dried using an absorbent wipe. The swollen mass was then recorded. Swelling is calculated as the mass change from dry to swollen normalized to the dry mass.

2.3.4 Biocompatibility Test of Polymers

A neuroepithelial cell line NE-4C (CRL-2925, ATCC, Manassas, VA) was used and maintained accordingly in ATCC-formulated Eagle's Minimum Essential Medium (Cat#30-2003, ATCC, Manassas, VA) supplemented with additional 2mM L-glutamine, 10% fetal bovine serum (FBS) and 1x Penicillin-Streptomycin (Cat#15070063, Thermo Fisher, Waltham, MA). A total of 100,000 cells were seeded in each well and cultured in 37°C and 5% CO_2 incubator for 24 hours, with either the polymer (SP1, SP2, SP3, SP4) or control. Then, Hoechst 33342 (Cat#62249, Thermo Fisher, Waltham, MA) and Ethidium Homodimer-III (EthD-III) (Cat#40050, Biotium, Fremont, CA) were added to differentiate all cells or dead cells, in which all cells were stained blue by Hoechst 33342 and dead cells were red by EthD-III. Nikon 90i live cell microscope was used for photography and ImageJ v1.53h was used for cell quantification.

2.4 Results and Discussion

2.4.1 Effect of Side Chain Length

To investigate the effect of side chain length on the transition temperature of the stiffness variable polymers, three different prepolymer solution were formulated as shown in **Table.1**.

Table 1 Formulations of prepolymer solutions for side chain length study
(weight ratio)

Samples	SA	HA	TA	UDA	TMPTA	DMPA
80% SA	80	0	0	20	1	1
80% HA	0	80	0	20	1	1
20% HA+60% TA	0	20	60	20	1	1

The 80% SA formula is the previously reported recipe^[21] for BS80, which has 80 weight parts of SA and 20 parts of UDA. The SA component in the prepolymer solution was replaced by a monomer hexadecyl acrylate (HA) with shorter side chain length (sample named 80% HA). The formula 20% HA+60% TA has 20 weight parts of HA, 60 weight parts of TA and 20 weight parts of UDA. With the addition of tetradecyl acrylate, the alkyl side chain length in this copolymer was further decreased. The prepolymer solutions were fully mixed and UV cured.

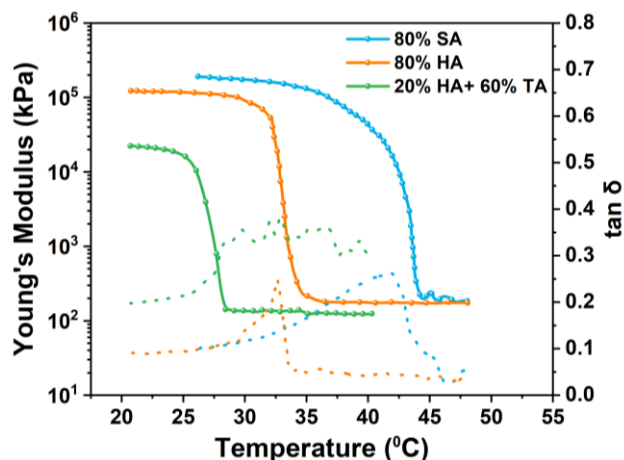


Figure 2.3 Modulus vs. temperature for polymers with different crystallizable side chains.

Fig. 2.3 shows the modulus vs. temperature of the three different polymers. As the HA replacement of SA, the transition temperature decreased from 43 °C to 35 °C. The transition range also narrows down from 7 °C to 3 °C due the closely packed crystalline domain and narrower distributed crystalline size at the terminal parts of the n-alkyl chain.^[58] With the adding of TA, the transition temperature was further decreased below 30 °C because of the lower melting temperature from the monomer, which is consist with similar polymers systems reported before.^[59] The results suggest that the length of the side chain can be used to tune the transition temperature of this stiffness variable polymer system. By controlling the weight ratio of SA, HA and TA in the prepolymer mixture, the transition temperature could be precisely controlled and lowered to body temperature range.

2.4.2 Effect of Crosslinker TMPTA

Trimethylolpropane triacrylate (TMPTA) is commonly used as a trifunctional small molecule crosslinker in polymer network. In the previous BS80 polymer system, the polymer serves as a dielectric elastomer which can be actuated in response to electrical field. Therefore, the polymer needs to be crosslinked to a certain degree to ensure fully recovery of the strain and low viscoelasticity of the material to overcome electromechanical instability. In the body temperature triggered stiffness variable polymer, we explored the effect of TMPTA in terms of modulus change and stress strain behavior.

Table 2 Formulations of prepolymer solutions for TMPTA study
(weight ratio)

Samples	HA	UDA	TMPTA	DMPA
0% TMPTA	80	20	0	1
1% TMPTA	80	20	1	1
2% TMPTA	80	20	2	1

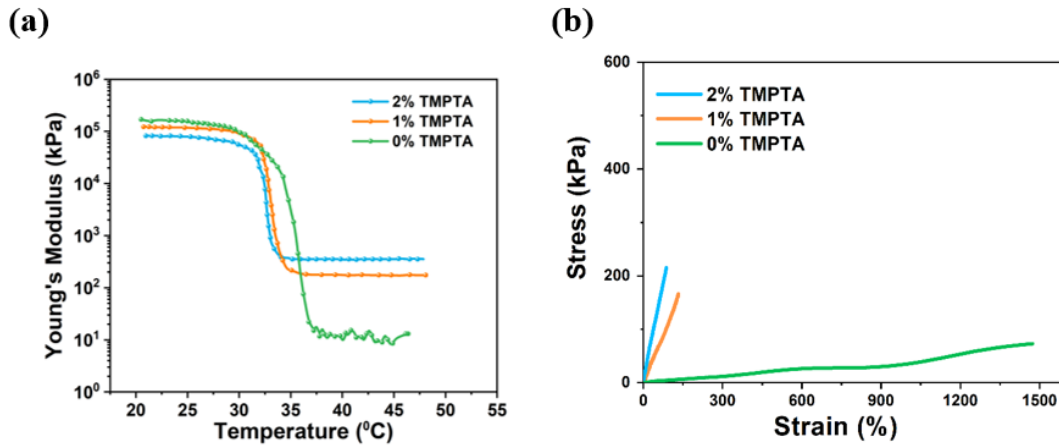


Figure 2.4 (a) Modulus vs. temperature and **(b)** Stress-strain curve of the polymers with different TMPTA percentage.

Three prepolymer solutions were formulated with different TMPTA weight ratio (shown in **Table. 2**). After polymerization, the Young's moduli of the polymers were measured by DMA. As shown in **Fig. 2.4 (a)**, when TMPTA percentage was increased from 1% to 2%, the modulus at soft state increased from 170 KPa to 350 KPa, due the increased crosslinking density of the elastomer. However, the modulus of the 2% TMPTA sample at rigid state is smaller than that of 1% sample.

This is because the increased percentage of the TMPTA makes the polymer main chain less flexible. And less flexible main chain would be unfavorable to the side-chain crystallization by not allowing the side chains to adjust their conformation to be packed closely. Therefore, less crystallization will be expected. This also indicates why the transition temperature shifts to the right with the TMPTA addition.

On the other hand, the polymer without addition of TMPTA ensures the maximum flexibility of the main chain. Crystallizable side chains can adjust the conformations for close packing with minimal disruption of regularity. The Young's modulus of 0% TMPTA sample is the highest among the three formulations. Meanwhile, the Young's modulus of 0% TMPTA sample can reach to 10 KPa range in the soft state. This is quite unique compared with common elastomers. Common elastomer networks are subject to intrinsic chain entanglements between their strands, which sets a preordained lower limit for the Young's modulus $\sim 10^5 - 10^6$ Pa.^[60] But in this HA-based polymer system, the comb-like, densely linked side chains make it bottlebrush polymer. The steric repulsions due to the side chain effectively eliminate the intrinsic chain entanglements^[20]. That is the reason why such bottlebrush polymers with no TMPTA crosslinker are able to reach kPa range in Young's modulus.

The removal of TMPTA also significantly increases the elongation at break of the HA based polymer, to over 1200%. Because of the decrease of crosslinking density, the polymer network is less vulnerable to the breakage of the bonds. However, if TMPTA is added, the tensile stress of the polymer is enhanced, as shown in **Fig.2.4 (b)**. In conclusion, TMPTA can decrease the modulus change ratio and elongation at break, but increase the tensile stress of these polymers.

2.4.3 Effect of Acrylic Acid

Acrylic acid (AA) with carboxylic group helps to form the hydrogen bonds in between the polymer network. Therefore, it is usually added into hydrogels or polymer networks to enhance the mechanical properties. We studied the effect of AA in transition temperature and the stress-strain behavior.

Table 3 Formulations of prepolymer solutions for AA study
(weight ratio)

Samples	HA	UDA	TMPTA	DMPA	AA
0% AA	80	20	1	1	0
5% AA	80	20	1	1	5
10% AA	80	20	1	1	10

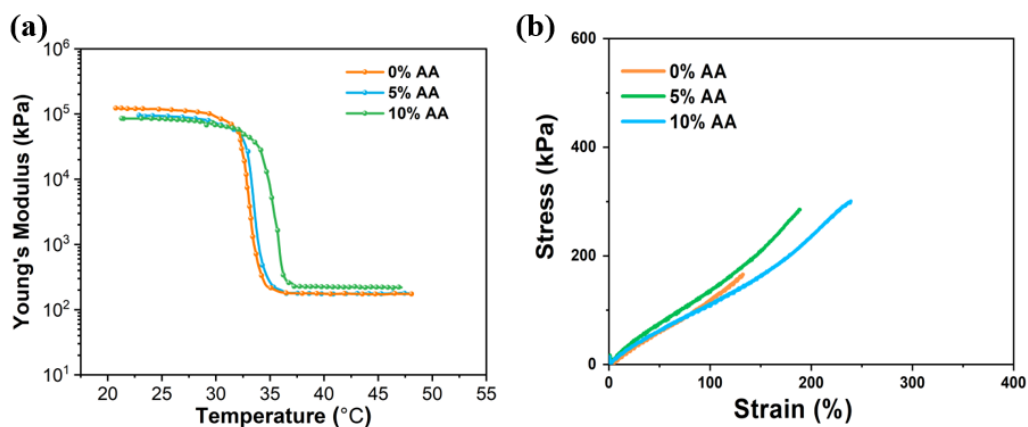


Figure 2.5 (a) Modulus vs. temperature and (b) Stress-strain curve of the polymers with different AA percentage.

Weight percentage variation was created in the HA-based prepolymer solutions from 0% AA added to 5%, and 10% AA added. After UV polymerization, the mechanical properties were characterized by DMA.

It is shown in **Fig. 2.5 (a)** that, the transition temperature shifts to higher temperature with more AA. And transitional range is also broadened with the increasing amount of AA, because the hydrogen bonding between the carboxylic groups enhances the inter-chain interactions, and the copolymerization influence the uniformity of crystalline domain. The elongation at break as well as the tensile stress both increased with increasing AA addition, due to the dynamic dissociation and reformation absorbs more energy when the polymer is under stretching.

However, it should also be noted that the acrylic acid with carboxylic group can absorb water.^[61] Therefore, for purpose of lower swelling rate, the comprehensive effect of AA should be considered.

2.4.4 Body Temperature Triggered Stiffness Variable Polymers for Bio Application

Based on the preliminary studies discussed above, in order to develop more smart devices based on body-temperature triggered stiffness variable polymers, we formulated a series of polymers with controlled softening temperature covering the body temperature range. **Table 4** summarized the softening polymers (SP), namely SP1 to SP4.

The polymers consist of different percentage combinations n-alkyl acrylates crosslinked by macro-crosslinker UDA. The resultant polymers are bottlebrush elastomers with crystallizable side chains. Below the transition temperature, the side chains forms nanocrystalline domain for the rigidity of the polymer network. Upon exposure to body temperature, the nanocrystalline domain melts and the bottlebrush system leads to kPa range Young's moduli.

Table 4 Formulations of prepolymer solutions for various softening polymer
(weight ratio)

Samples	SA	HA	TA	UDA	DMPA
SP1	0	60	20	20	0.5
SP2	0	80	0	20	0.5
SP3	10	70	0	20	0.5
SP4	20	60	0	20	0.5

It is shown in **Fig. 2.6 (a)** that the four softening polymers with different compositions have different transition temperature. A prior study demonstrated that the reactivity ratios of the various combinations of acrylate monomers were unity, which means that the polymer compositions can be taken to be equal to the monomer concentrations^[62]. The mechanical properties of the four polymers were characterized by DMA.

Table 5 Transition temperatures and moduli of the softening polymers

Samples	T_m (°C)	Young's Modulus (kPa) @20°C	@40°C	Modulus Change Ratio
SP1	32.2	1.22×10^5	10.7	11,300
SP2	36.5	1.99×10^5	10.6	18,800
SP3	37.1	2.10×10^5	20.0	10,500
SP4	39.9	2.21×10^5	47.8	4,600

Table 5 summarized the transition temperatures and moduli of the four softening polymers. Among the four samples, Among the polymers, SP1 with shorter side chain length has lowest transition temperature at 32.2 °C, which corresponds to the skin temperature range. SP2 has transition temperature at 36.5 °C. For SP3 and SP4, the transition temperatures are 37.1 °C and 39.9 °C respectively. The largest modulus change ratio comes from the polymer SP2, with 18800× variation in a sharp range ~3°C.

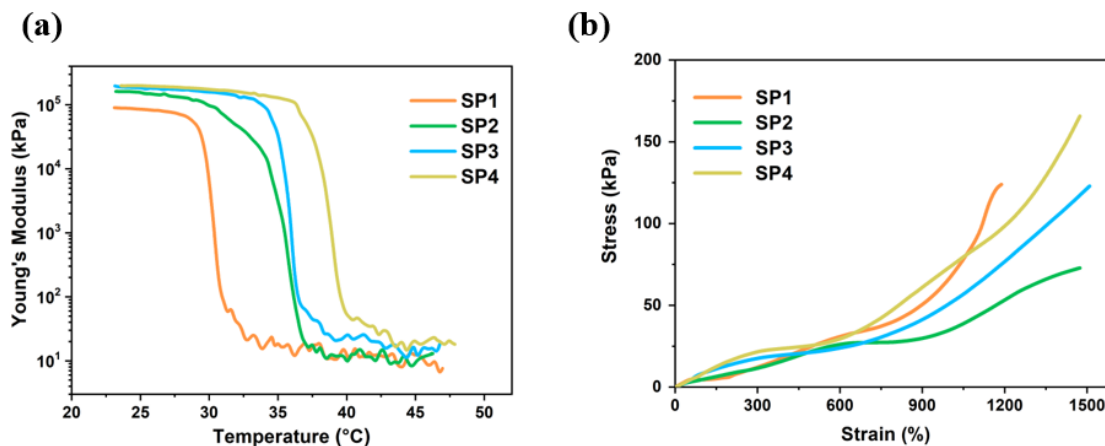


Figure 2.6 (a) Modulus vs. temperature and **(b)** Stress-strain curves of the polymers SP1 to SP4 with different transition temperature.

Fig. 2.6 (b) shows the uniaxial stress-strain curve of the four softening polymers (SP1-SP4) measured at 45 °C. The polymers are soft and highly stretchable above transition temperature, and they can achieve a maximum elongation at break larger than 1000%.

Wide angle X-ray diffraction (**Fig. 2.7**) has revealed these poly(*n*-alkyl acrylates) are paraffin-like crystalline forming hexagonal crystal lattice structures. This verified the nanocrystalline domain formed by the side chain of the polymers. The four polymers all have very sharp transition range within 3°C thanks to the narrow size distribution of crystallites. The layered structure with hexagonal arrangement of the long hydrocarbon chains can be deduced from the XRD. The long alkyl chains in poly(*n*-alkyl acrylates) were suggested to form inverse combs in the planar polymer chain structure while the layered polymer chains stacked to give a 3D layer-by-layer ordered structure.^[63]

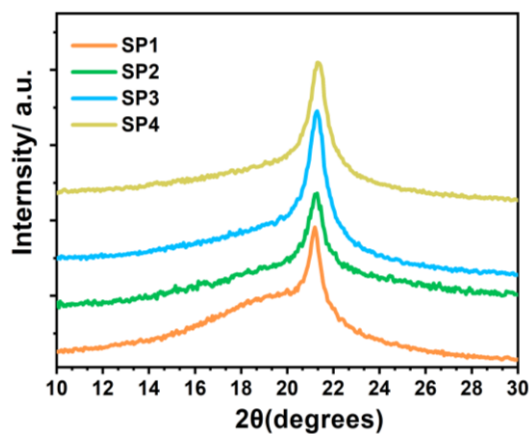


Figure 2.7 Wide angle X-ray diffraction of the softening polymers with the crystalline domain

Fig. 2.8 shows DSC traces for the softening polymers upon heating. The sharp endothermic peaks were observed, which can be ascribed to the melting of crystallized n-alkyl chains. The peak top (melting temperature) shifts to the higher temperature with increased side chain length. It is also showed that the area of the endothermic peak increases with longer side chains.

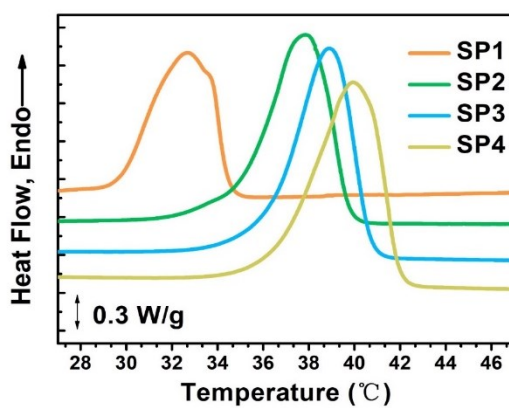


Figure 2.8 DSC of the four softening polymers showing the phase transition properties of the polymers.

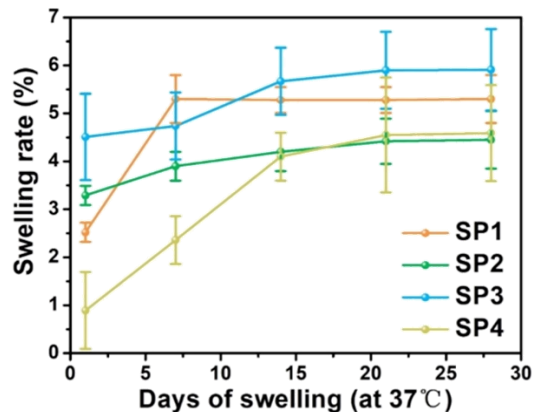


Figure 2.9 Swelling rate of softening polymers in phosphate-buffered saline at 37 °C.

Swelling rate of the four softening polymer films was measured after immersion in phosphate-buffered saline (PBS) for a period of time at 37 °C. PBS is an isotonic solution used in many biological research applications to mimic the body fluid environments. The implanted materials for neural interface application should remain stable in body fluid. The swelling rate after soaking is shown in Fig. 2.9. All polymers have relatively low swelling ratio below 7%. The relatively low swelling ratio is contributed to the densely linked hydrophobic alkyl side chains of the polymers. In the meantime, no degradation of the polymers was observed. This indicates the softening polymers as substrates can maintain good geometrical stability in physiological environments.



Figure 2.10 Photos of the polymer SP2 softening on a rat brain.

To demonstrate the softening polymer can adapt to the softness of tissue at body temperature, we put a SP2 polymer film on top of the brain tissue of a rat. The polymer softened quickly once in contact with the brain tissue and conformed to the curvature of the brain within 10 s, forming an intimate wrap-around contact (**Fig. 2.10**). The softened polymer also shows strong adhesion due to their super high softness that ensures maximum surface contact above transition temperature.

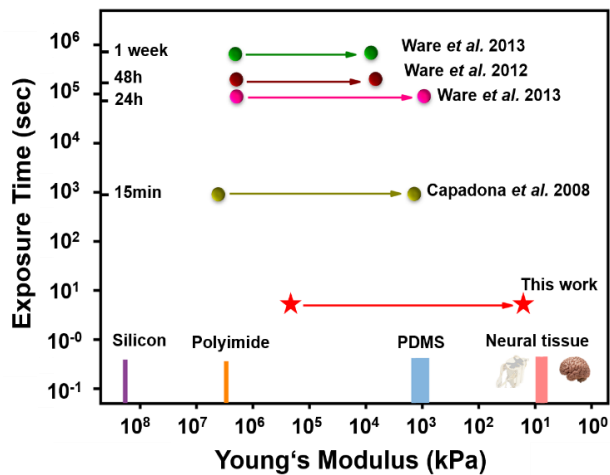


Figure 2.11 Comparison of Young's moduli and softening response time between previously reported materials and softening polymers developed in this work (bottom, red).

Compared with previously published softening polymers, our softening polymer SP2 softens within 10 seconds, and no water-assisted process is needed since the softening mechanism is based on melting of crystalline domain, instead of water plasticization (Fig. 2.11). More importantly, our softening polymer can adapt to the Young's modulus of soft nerve tissue in kPa range due to the bottlebrush polymer network. This will be a huge benefit for real tissue-like electronics and neural interfaces.

2.4.5 Biocompatibility Evaluation

For implantable neural interfaces, a cell compatible biomaterial that has negligible cytotoxicity is required. To test the cell viability when cells are in coculture with the four softening polymers, a neuroepithelial cell line NE-4C was cultured at 37 °C for 24 hours, with either the polymer (SP1, SP2, SP3, SP4) or media-only control. A total of 100,000 cells were seeded in each well and cultured in 37 °C and 5% CO₂ incubator for 24 hours. Then, Hoechst 33342 and Ethidium Homodimer-III (EthD-III) were added to differentiate all cells or dead cells, in which all cells were stained blue by Hoechst 33342 and dead cells were stained red by EthD-III.

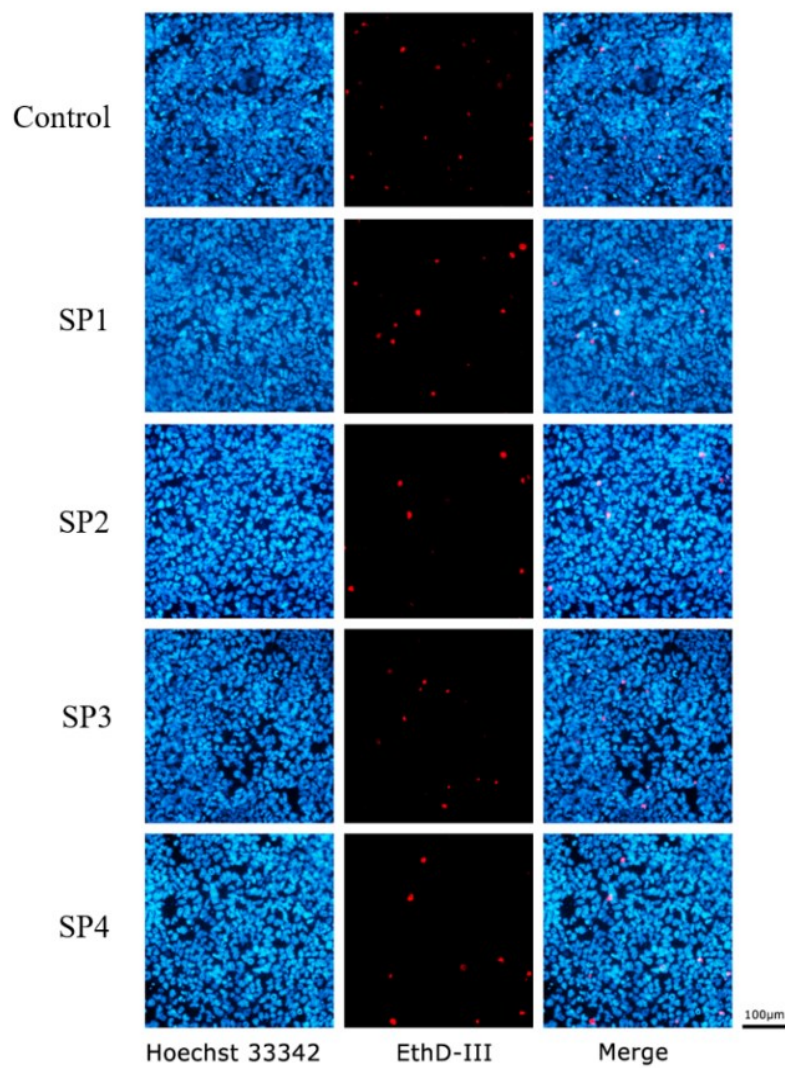


Figure 2.12 Microscopic image of labeling of neuroepithelial cell NE-4C after 24 hours coculturing with softening polymers.

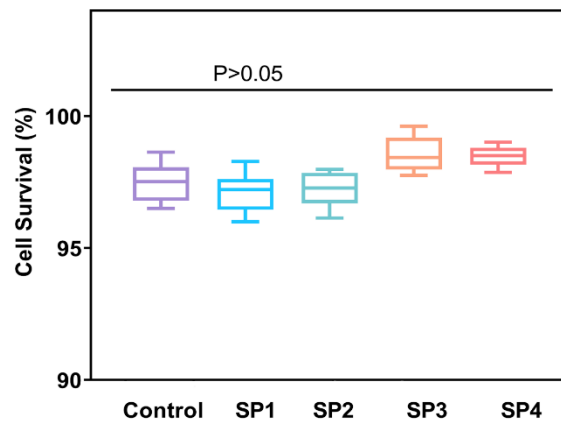


Figure 2.13 Evaluation of neuroepithelial cell NE-4C's survival in response to the polymer (SP1, SP2, SP3, and SP4) and control materials.

As shown in **Fig. 2.12** and **Fig. 2.13**, all four softening polymer provided good cell viabilities to the cells. No significance difference was found in the survival rate of softening polymers compared with the media-only control. This preliminary result suggests that the softening polymers are not cytotoxic and can be used as neural interfaces.

2.5 Conclusion

Within the poly(n-alkyl acrylates) stiffness variable polymer system, the effect of side chain length was studied. The decrease of n number in the side chain has shown decreased transition temperature to body temperature range. The removal of small molecule crosslinker TMPTA from the polymer system enlarges the modulus change ratio. Subsequently, a series of body temperature triggered stiffness variable polymers were formulated, with transition temperature from 32 °C to 40 °C. The softening of the polymers comes from the melting of the nanocrystalline domain from the side

chains. These polymer shows large moduli change ratio, sharp and fast rigid-to-soft transition, and no cytotoxicity to the neural cells. They can be potentially used as substrates for thermal-responsive, mechanically adaptive neural interfaces, which are rigid before implantation and become soft after implantation.

Chapter 3. Thermal-responsive, Mechanically

Adaptive Neural Probes

3.1 Introduction

As mentioned in Chapter 2, the next generation neural interfaces should have mechanical stiffness close to nerve tissues for intimate contact and stable electrical communication. With the body temperature triggered stiffness variable polymers that can be softened to kPa-range softness, opportunities are provided to fabricate thermal-responsive, mechanically adaptive neural interfaces. The implantable smart devices would be stiff before and during implantation, and quickly become soft after implantation to eliminate the mechanical mismatch.

Apart from the mechanical mismatch challenge, neurological information processing involves action potentials along the axons and neurotransmitter release at the synapses. This multiplicity requires multifunctional probes to simultaneously measure or modulate diverse signals *in vivo*. However, there are only limited tools that can sense different signals simultaneously.

Serotonin, also termed 5-hydroxytryptamine (5-HT), is a key neurotransmitter related with mood adjustment and a potential target for treating mental disease. Specifically, in spinal cord, serotonin modulates sensory as well as autonomic functions, and facilitates motor output.^[64, 65] While many tools have been developed and applied for electrophysiology, limited tools are available for neurochemical monitoring.^[66-69] The capabilities to monitor both electrical and serotonin signal will provide unprecedented and powerful information to understand the neural functions.

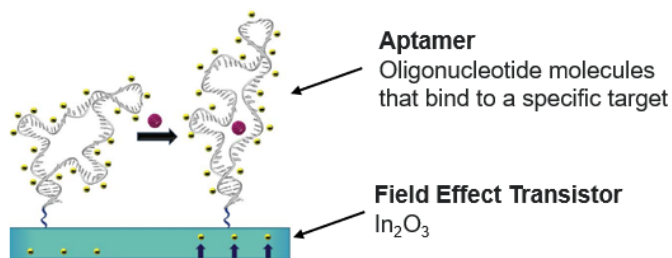


Figure 3.1 Mechanisms of sensing neurotransmitters based on the FET-Aptamer sensor reported before in Ref [71].

Previously, Andrews et. al reported In_2O_3 field-effect transistor (FET) biosensors for serotonin (**Fig. 3.1**) and other small molecules monitoring under high ionic concentrations.^[70-74] Aptamer-based FET sensors were shown to detect a variety of biomarkers, including dopamine, serotonin, glucose, and phenylalanine, in complex physiological environments such as brain tissue and blood serum.^[70-74] However, the substrates of these sensors which are silicon and polyimide are still several orders of magnitude stiffer than the soft neural tissue.

Therefore, it is of great interest to explore the application of our softening polymer in building multi-modal neural probes and sensors for neurochemical recording. For this purpose, we selected SP2 with transition temperature $36.5\text{ }^\circ\text{C}$ as our substrate for study. We proposed to fabricate different sensors to demonstrate the versatility of the polymer.

Compared with mature silicon substrates, soft substrates are often vulnerable to microfabrication process in terms of low yield and high failure rate. Because microfabrication often requires the substrate's exposure to organic solvents, water, baking or etchant. Yet polymers, with high

coefficient of thermal expansion, can have deformation during heating, or can swell in solvents. Incorporation of functional electronics into soft substrate, *e.g.*, FETs, is more challenging compared with conductive electrodes due to the complexity of semiconductor fabrication and integration. To evaluate whether our softening polymers can tolerate the microfabrication process and be used as a platform to build neural probes, we first demonstrated a simple intracortical array for electrophysiological recording, then designed and a multimodal neural probe integrating electrophysiological recording and serotonin sensing on SP2.

3.2 Proposed Methods

The body temperature triggered stiffness variable polymers have great promise to reduce the mechanical mismatch. But the device fabrication process on the polymer still needs to be studied. We designed a fabrication process (**Fig. 3.2**) with pattern transferred by polymerization and room-temperature semiconductor deposition for FETs integration. Briefly, Parylene-C encapsulation layer was first deposited on a clean glass slide, followed by deposition of conductive traces or semiconductors. Using this glass slide as the bottom of a mold, the prepolymer solution of SP2 is injected into the mold and polymerized. The pattern is then transferred to the softening polymer. The device is peeled off, flipped over and further defined. In this way, most of the process is done on rigid substrate. So that the patterning can be done with maximum precision.

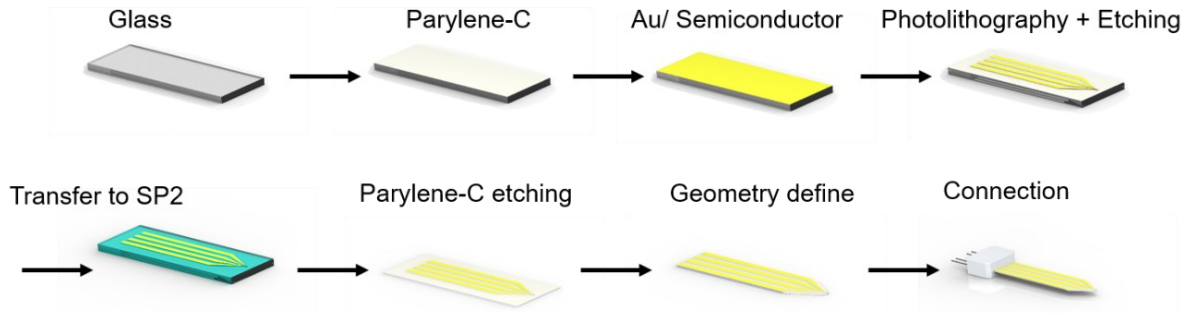


Figure 3.2 Fabrication process flow of building neural probes on the body temperature triggered softening polymer substate SP2.

Based on this fabrication method shown in **Fig. 3.2**, we proposed to build a simple intracortical probe using gold as the conductive traces. Meanwhile, to meet the multiplicity requirements of the neurological process, we also proposed to build multimodal probe integrating both electrophysiological sensing and neurotransmitter sensing functions on the thermal-responsive, mechanically adaptive polymers.

3.3 Experiment Section

3.3.1 Materials

Urethane diacrylate (UDA) CN9021 was generously provided by Sartomer Company (Exton, PA). Hexadecyl acrylate (HA) was purchased from TCI America (Portland, OR). 2,2-Dimethoxy-2-phenylacetophenone, Cr etchant, Ti etchant, (3-aminopropyl)triethoxysilane, trimethoxy(propyl)silane and 3-maleimidobenzoic acid *N*-hydroxysuccinimide ester were

purchased from Sigma-Aldrich (St. Louis, MO). Gold etchant TFA was purchased from Transene Company Inc (Danvers, MA). All chemicals were used as received without further purification.

Oligonucleotides were obtained from Integrated DNA Technologies (Coralville, IA). Serotonin aptamer oligonucleotide was: 5'-/5ThioMC6-D/CGACTGGTAGGCAGATAGGGGAA GCTGATTCGATGCGTGGGTCG-3'. Serotonin scrambled aptamer: 5'-/5ThioMC6-D/CCCGG GAATTCGGAATTGGGGCAATTGATGAGGGGGTCATGGG-3'. Dopamine aptamer: 5'-/5ThioMC6-D/CGACGCCAGTTTGAAGGTTTCGTTTCGCAGGTGTGGAGTGACGTCG-3'.

3.3.2 Fabrication of Intracortical Arrays on SP2

All fabrication steps except polymerization and laser cutting were performed in a Class 1,000 cleanroom. Glass microscope slides of 75 mm×50 mm were first cleaned by Alconox detergent (Alconox White Plains, NY) as well as repeated sonification in acetone and isopropanol. Then, 500 nm of Parylene-C was deposited in SCS Labcoater 2 Parylene Deposition System (PDS 2010, Specialty Coating Systems Inc., Indianapolis, IN). Metal layers of 20 nm thick Cr and 50 nm thick Au were then deposited using CHA Mark 40 (CHA industries, Inc., Fremont, CA) at the rate of 0.3 nm/sec. The metal electrode was then patterned by photolithography followed by wet etching using gold etchant and Cr etchant.

Using this electrode patterned glass slide as a bottom piece, another clean glass slide with Kapton spacer was taped together as a mold. Liquid prepolymer solution was prepared by mixing UDA, HA, and DMPA at the ratio listed for SP2. Prepolymer solution was heated to 60 °C and injected into the mold. The polymer solution was polymerized under 365nm UV light for 2 min. The mold

is then flipped over and cooled. Parylene-C side was separated from glass slide using a razor blade assisted with water. The parylene-C was etched by O₂ plasma on Technics Micro-RIE using a positive photoresist AZ4620 (MicroChemicals, Germany) as a mask. Excessive photoresist was washed off by another flood exposure followed with development. The probe tip was cut by 30W Epilog Zing CO₂ laser cutter and then the probe was inserted into ZIF connectors (Part#39532054, Molex, USA).

3.3.3 Fabrication of Multimodal Neural Probes on SP2

A 500 nm thick Parylene-C was deposited on a cleaned glass slide using SCS Labcoter 2 Parylene Deposition System (PDS 2010, Specialty Coating Systems Inc., Indianapolis, IN). Metal electrodes of 20 nm thick Ti and 50 nm thick Au was deposited using CHA Mark 40 (CHA industries, Inc., Fremont, CA) at the rate of 0.3 nm/sec. The metal electrode was patterned by photolithography followed by wet etching using gold etchant and Ti etchant. A 20-nm thick In₂O₃ was sputtered onto the patterned electrodes using room temperature radio frequency (RF) sputtering (Denton Discovery Sputter, Denton Vacuum, LLC, Moorestown, NJ), and defined by a photoresist lift-off process. Using this glass slide as the bottom of the mold, mixture of SP2 prepolymer solution was injected and cured under same condition described before. The parylene-C was protected using AZ4620 as mask and etched by O₂ plasma to expose the recording site (diameter 30 μm) as well as the In₂O₃ window (120 μm×120 μm). Excessive photoresist was washed off by another flood exposure followed with development. The probe was defined by laser cutter and then inserted into the ZIF connector. Before functionalization with aptamer, the two electrodes for electrophysiological recording were covered with PDMS masks to avoid

contamination. The polymer devices were rinsed in ethanol and dried with N₂ to clean the surface. After thorough cleaning, (3-aminopropyl)triethoxysilane and trimethoxy(propyl)silane (1:9, v/v) were deposited on the In₂O₃ surface at room temperature by vacuum chamber for 4 h, and then annealed at ambient environment overnight. The devices were immersed in a solution of 1 mM of 3-maleimidobenzoic acid *N*-hydroxysuccinimide ester dissolved in a 1:9 (v/v) mixture of dimethyl sulfoxide and phosphate-buffered saline (PBS, Gibco, Fisher Scientific, Waltham, MA) for 30 min. After rinsing with deionized (D.I.) water, the devices were immersed in a 1 μM solution of thiolated aptamer in PBS overnight. Devices were rinsed with D.I. water and dried with N₂ before measurements.

3.3.4 Preparation of Brain Phantom for *In Vitro* Study

Agarose was purchased from Sigma-Aldrich (St. Louis, MO). 0.6% agarose water solution were prepared as a brain phantom. The agarose solutions were heated and poured into a Pyrex petri dish to cool and solidify at room temperature.

3.3.5 Electrochemical Impedance Spectroscopy (EIS)

The EIS measurements were performed in PBS at room temperature by using a potentiostat (Princeton Applied Research Versastat 3, Ametek, USA). The test was set up in that the fabricated probe on SP2 substrate served as a working electrode, Pt wire as counter electrode and an Ag/AgCl as reference electrode (saturated KCl-AgCl solution). A 10 mV RMS sinusoidal signal ranging from 100 kHz to 10 Hz was sent to the device.

3.3.6 Surgical Implantation of Intracortical Probe

Sprague dawley rats (270-300 g body weight) were used for *in vivo* implantation and recording experiments. The rats were housed individually with food and water provided. All surgical procedures were conducted under aseptic conditions with the rats deeply anesthetized with isoflurane gas administered via facemask as needed. All procedures described below are in accordance with the National Institutes of Health Guide for the Care and Use of Laboratory Animals and were approved by the Animal Research Committee at University of California, Los Angeles.

The scalp was first shaved and the skin was removed from the skull area. Craniotomy were performed for the insertion tests. Selected hindlimb muscles, i.e., the tibialis anterior and soleus, were implanted bilaterally with intramuscular EMG recording electrodes. Skin and fascial incisions were made to expose the belly of each muscle. Two wires extending from the skull-mounted connector were routed subcutaneously to each muscle. The wires were inserted into the muscle belly using a 23-gauge needle, and a small notch (approximately 0.5–1.0 mm) was removed from the insulation of each wire to expose the conductor and form the electrodes. The wires were secured in the belly of the muscle via a suture on the wire at its entrance into and exit from the muscle belly.

The intracortical probe was vertically mounted on a micromanipulator and positioned in the motor cortex. The insertion was performed at speed ~1mm/s, 1mm deep. To implant the stimulating wire electrode in the dorsal epidural space, a T12 to L2 vertebrae laminectomy was performed to expose the spinal cord. After epidural placement, the array was covered with small cotton balls rinsed in

saline. A common ground was inserted in the back. Following the recording electrodes implantation, voltage signals from the intracortical probe were amplified and digitized at 40KHz using bioamp and powerlab Data Acquisition System (ADInstruments). The animal was anesthetized with 1.5% isoflurane in medical-grade O₂ during the whole measurement. A 1000Hz high-pass filter and a 60-Hz notch filter were applied for single-unit recording. Spike detection were performed using labchart pro (ADInstruments) software.

3.3.7 *Ex vivo* Experiments for Serotonin Sensing

Brain tissue lacking serotonin was obtained from *Tph2* knockout mice. The brains were obtained from the laboratory of Dr. Donald Kuhn (Wayne State University, Detroit, MI) and were shipped under dry ice. Brain tissue collection procedures were approved by the Wayne State University Institutional Animal Care and Use Committee.

Brain tissue was stored at -80 °C before experiments. Tissues were homogenized in artificial cerebrospinal fluid (aCSF) 1:1 volume ratio on ice using a VirTis Virsonic600 ultrasonic cell disruptor (Gardiner, NY). Commercially available Ag/AgCl reference electrodes (Super Dri-Ref, World Precision Instruments, Inc., Sarasota, FL) were placed in the tissue homogenates above the FETs. All FET measurements were performed using a Keithley 4200A (Tektronix, Beaverton, OR) semiconductor analyzer. Source-drain current (I_{DS}) transfer curves were obtained by sweeping the gate voltage (V_{GS}) from 0 to 400 mV while maintaining the drain voltage (V_{DS}) at 500 mV.

3.4 Results and Discussion

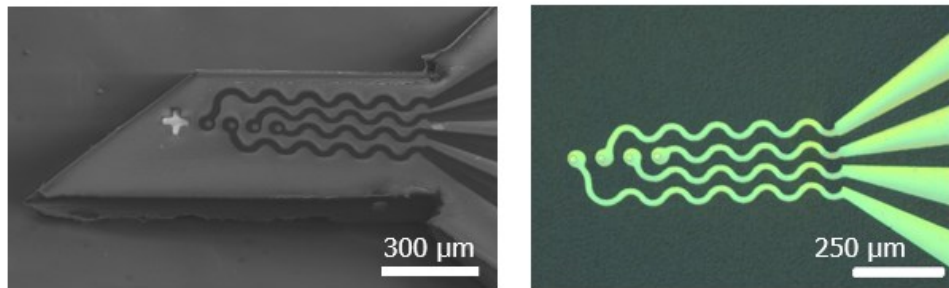


Figure 3.3 Scanning electron microscope image of the intracortical probe (left) and the optical microscope image of the conductive electrode traces (right)

With the microfabrication process flow described above, the thermal-responsive mechanically adaptive intracortical probes were successfully developed based on the stiffness variable polymer SP2. **Fig. 3.3** shows a fabricated intracortical probe on softening polymer SP2 under scanning electron microscope and optical microscope. To realize multiplexed recording of neural signal, four recording sites were designed to be 50 μm in diameters (exposed recording areas without Parylene-C insulation were 30 μm in diameter) and 80 μm apart to access different level of neurons. The successful fabrication of the intracortical electrode on thermal-responsive substrate proved that with the current process control, the softening polymer can be compatible with the microfabrication process (including photolithography and etching) and to be used as substrates for microelectronic devices.

3.4.1 Insertion Buckling Assessment

As discussed in Chapter 1, efforts have been made to minimize the microelectrode footprint and eliminate the mechanical mismatch. However, a challenge still remains that during insertion, the device must be stiff enough to prevent early buckling and pierce into the brain tissue. To assess the insertion success rate of the softening polymer-based electrode as well as finding the minimal thickness without buckling, *in vitro* and *in vivo* insert tests were performed.

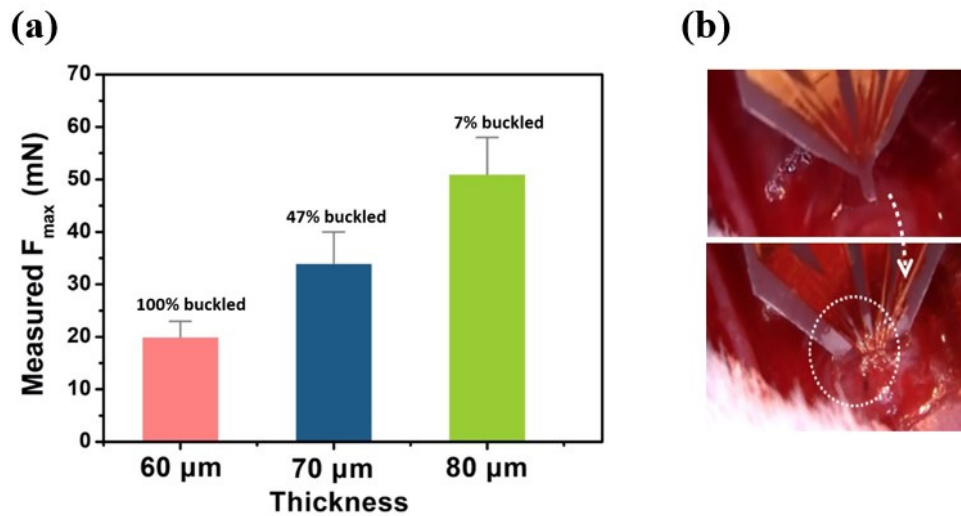


Figure 3.4 (a) Maximum force before buckling of different thickness of SP2 strips and buckling rate of insertion into 0.6% agarose tissue phantom ($n=15$ for each thickness). **(b)** Photos of the penetration of the softening polymer probe into rat brain.

To simulate the stiffness of the brain, 0.6% agar gel was prepared as tissue phantom.^[75] The modulus of the 0.6% agar gel is around 14 kPa.^[76] Intracortical probes (1 mm \times 300 μm) with

different thickness were fabricated and inserted using a micromanipulator at a speed of 1 mm/s into the brain phantom. A successful implantation was defined as insertion without any buckling or early softening of the probe. Fifteen trials were performed for each thickness. Standard compression tests against a hard substrate were also performed on DMA to measure the highest force (F_{\max}) that a sample can withstand before failure. The results are shown in **Fig. 3.4 (a)**. For 60 μm thick devices, the measured F_{\max} is less than 20mN, and buckling was observed in all devices during insertion. For 70 μm thick devices, the buckling rate was 47%. Increasing the thickness to 80 μm , a success insertion rate of 93% was achieved with a maximum force of 48 mN. To ensure all fabricated neural probes on SP2 substrate can be inserted without buckling, 85 μm was selected as the probe substrate thickness for *in vivo* tests.

In vivo insertion evaluation was performed on sprague dawley rat with dura removed. The probes were inserted into the brain with a micromanipulator at the speed $\sim 1\text{mm/s}$, as shown in **Fig. 3.4 (b)**. The probe's penetration into rat brain tissue was smooth, without any buckling ($n=12$). No early softening during the insertion or partial insertion was observed. The success insertion using softening electrodes makes it possible for subsequent *in vivo* neural recording in rat.

3.4.2 Finite Element Analysis

A 3D finite-element model of the probe–tissue interface was built to compare the softening polymer and polyimide in reducing the strain around the tip. The quarter-symmetric model was built in ANSYS 2020 R2 (Canonsburg, PA) with a shank probe (orange) inserted into brain tissue (blue). Pre-simulation conditions were defined such that the probe was in contact with the brain tissue, with the friction coefficient of 0.1.

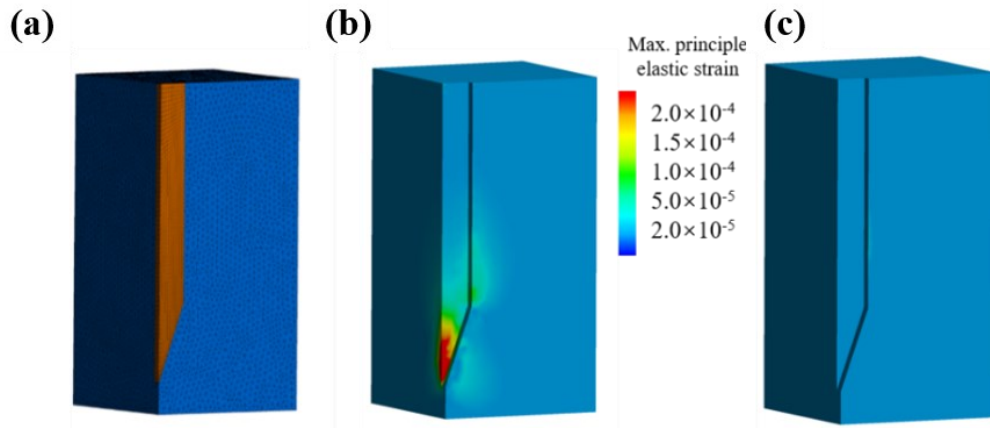


Figure 3.5 (a) 3D quarter-symmetric finite element model with a shank probe (orange) inserted into brain tissue (blue). Strain profiles induced in the brain tissue by 20µm displacement with (b) polyimide probe and (c) the softening polymer.

Table 6 Summary of FEA parameters

Part	Dimensions (mm)	Young's Modulus (kPa)	Poisson's ratio
Brain	0.75(l)×0.75(w)×1.50 (h)	6.0	0.45
Polyimide probe	Quarter-symmetric 1.36(l)×0.13(w)×0.04(t)	2.79×10^6	0.27
Softening polymer probe	Tip angle 20°	15.0	0.33

Table 6 summarized the materials properties used for the brain, polyimide probe and the softening polymer probe (at the soft state). Boundary conditions were defined as follows: the bottom surface of the tissue was fixed in the simulations, preventing large scale global displacements while allowing local displacements around the implant site. The back end of the probe was displaced by 20 µm upward.

The strain comparison is between traditional flexible substrate polyimide and the softening polymer above transition temperature. The maximum principle elastic strain for polyimide and softening polymer probe are shown in **Fig 3.5 (b)** and **Fig. 3.5 (c)**, respectively. The simulation results indicated that softening substrates could reduce the elastic strain caused by micromotion at the probe–tissue interface. Presumably, these reduced strains should result in less inflammatory response and glial sheath formation around the implant.^[77, 78]

3.4.3 *In vitro* Strain Field Characterization

To compare the effect of the mechanically adaptive polymer with traditionally used flexible substrate polyimide in reducing micro-strain, *in vitro* strain field measurement was done in brain phantom. First, dummy probes with 85 μm thick polyimide or SP2 substrate were first defined by CO₂ laser cutter. The agarose gel was heated to 37 °C before the test. The probe was linked to a manual micro stage (Optics Focus, China). After insertion, the probe was displaced 20 μm by the micro stage in the axial directions to simulate micromotion.

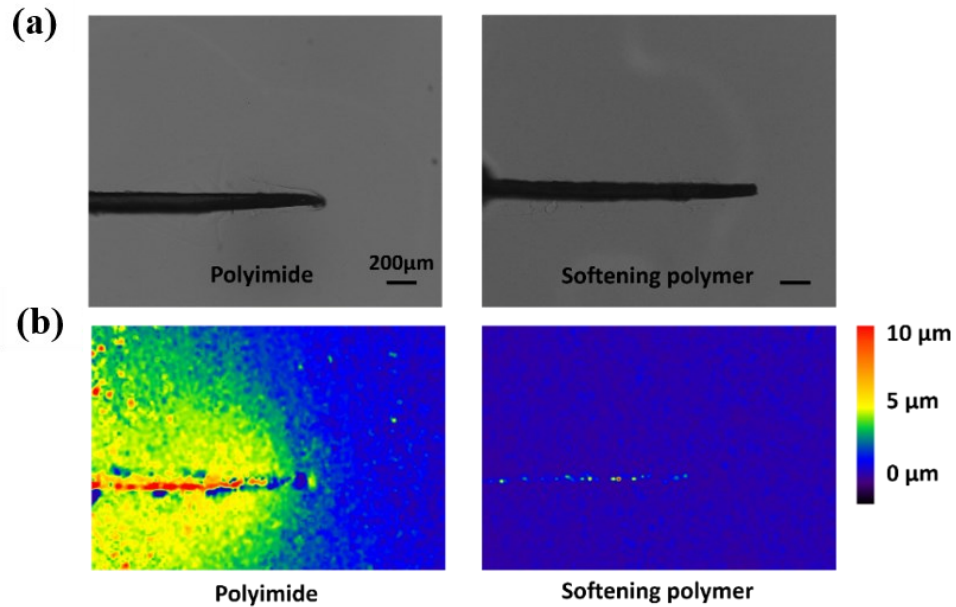


Figure 3.6 *In vitro* strain field characterization. **(a)** Bright field images of a dummy polyimide probe and softening polymer SP2 probe inserted into the agarose tissue phantom. **(b)** Strain field plots after a 20-micron axial displacement was applied to devices to mimic micromotion from accelerations.

A series of bright field images were obtained before and after displacement. The images were then analyzed using ImageJ: Particle Image Velocimetry (PIV) plugin to construct the displacement fields and shown in **Fig. 3.6 (b)**. On the left side, the polyimide-based probe has much higher displacement introduced to the brain phantom. While the softening polymer become super soft and stretchable, thus buffering the external micromotion. The resultant displacement is much smaller.

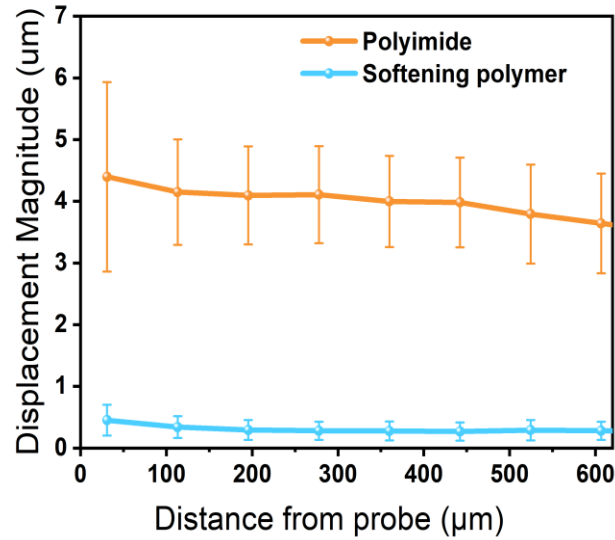


Figure 3.7 Average profiles of the displacement magnitude as a function of distance from the device for polyimide and softening polymer SP2.

Fig. 3.6 and **Fig. 3.7** suggest an obvious reduction in the local strain field around mechanically adaptive probe tip with softening polymer compared with polyimide tip. The softening polymer-based probe tip have reduced strain for all distances from the device. The average displacement at the surface of the polyimide probe tip was $4.5 \pm 1.5 \mu\text{m}$, while the softening polymer reduced the surface displacement to $0.45 \pm 0.25 \mu\text{m}$.

The result of the strain field study further validates the polymer can be softened by body temperature to adapt to the tissue softness inside the 37°C brain phantom. It also clearly confirms the reducing the Young's modulus of the substrate reduces the local strain around the device, which is in consistent with the FEA strain simulation.

3.4.4 Electrical Impedance Characterization *In Vitro*

Lower impedance and stable electrical connection are needed for recording of neural signals with high signal to noise ratio. We performed *in vitro* impedance measurement in PBS to evaluate the fabricated probes. The average of impedance of the gold-based probe at 1 kHz is $490 \pm 71 \text{ k}\Omega$ (n=8).

To test the robustness of the probe on the thermal responsive, mechanically adaptive polymers, we measured the impedance changes after bending tests. The probe tips were repetitively bent to a rod with radius of 0.5 mm. As shown in **Fig. 3.8**, the impedance remains relatively stable after 4000 bending cycles. The impedance after 4000 bending tests increased less than 20% at 1kHz.

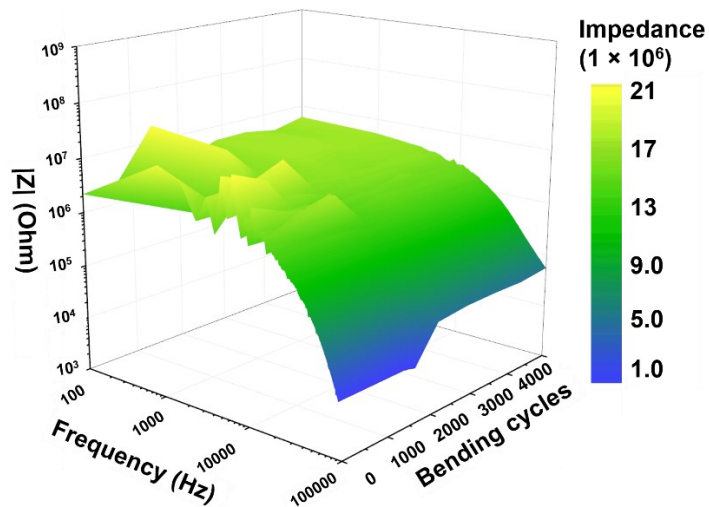


Figure 3.8 Impedance map after bending cycle tests with 0.5 mm bending radius at different frequencies.

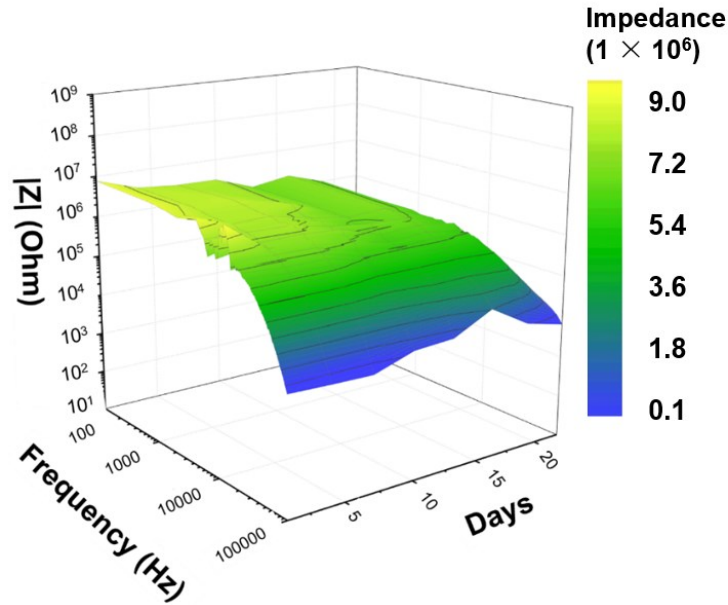


Figure 3.9 Impedance map of the fabricated intracortical probe after soaking in PBS for 19 days.

We also performed impedance measurement after soaking in PBS. The result is shown in **Fig. 3.9**. The electrical impedance of the intracortical probe gradually saturated as being immersed in phosphate-buffered solution (PBS) solution for 19 days. No delamination nor degradation of the probes on SP2 substrate was observed, which indicates the stability of the softening polymers as substrate for neural interfaces.

3.4.5 *In Vivo* Electrophysiological Recording

We did acute *in vivo* experiment using the thermal-responsive intracortical array to record the neural activity in rat brain. The intracortical probe based on SP2 substrate was successfully inserted into the motor cortex. In the meantime, a stainless steel wire was implanted over the dura at spinal

cord level S1 for stimulation. Bipolar electromyogram (EMG) electrodes were implanted in the belly of select hindlimb muscles. The setup of the experiment is shown in **Fig. 3.10**.

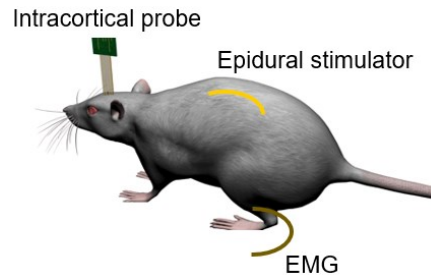


Figure 3.10 Schematic illustration of the *in vivo* experiment using softening polymer based intracortical array for neural activity recording.

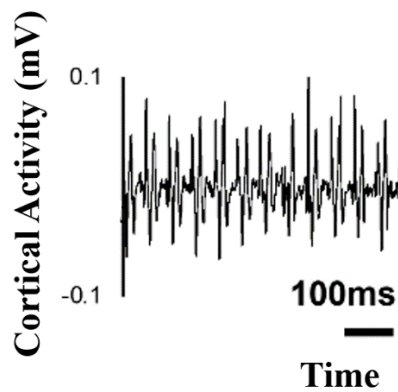


Figure 3.11 Recorded signal of repetitive firing shows amplitude accommodation typical of excitatory neurons.

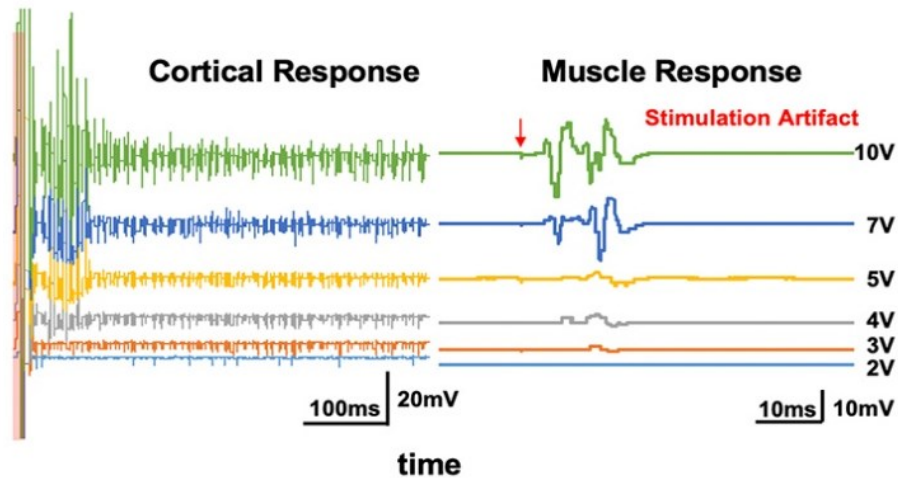


Figure 3.12 Electrophysiology recording of cortical response with respect to leg muscle movements in response to spinal cord stimulation.

After the probe insertion, *in vivo* neural recording in rats was performed. The cortical activity was recorded on four electrodes. Representative recorded *in vivo* cortical signals at rest are shown **Fig. 3.11**. Multiple unique spikes were detected on each channel based on the shape and amplitude of the spike.

In addition, the probe was also used to record cortical activity during activation of the hindlimb muscles. As shown in **Fig. 3.12**, the polymer probe monitored cortical responses corresponding to the electrical stimulation pulses delivered to the lumbosacral spinal cord was implanted over the dura at spinal cord level S1. Bipolar EMG electrodes were implanted in the belly of select hindlimb muscles^[79] and recorded in sync with the polymer electrodes in the cortex. Then, a series of continuous monophasic rectangle waves of varying voltage (2 V to 10 V) were delivered to the spinal cord through a stainless steel epidural spinal cord wire electrode. By delivering the electrical

stimulation, we observed bidirectional activation of the neural networks resulting in retrograde to the motor cortex and simultaneously anterograde to the hindlimb muscles. Unique intensity dependent evoked responses were recorded both in the EMG electrodes and in the cortex. The waveforms recorded are similar, while the peak potentials increase with increasing applied voltage amplitudes, which are consistent with the literatures.^[79-81]

The *in vivo* recording experiment showed the ability of the body temperature triggered softening polymer SP2 to be used for multiplexed recording in neural interfaces towards mechanically adaptive, tissue-like electronics.

3.4.6 Field-effect Transistor Based on the Thermal-responsive Polymer

In the study of tissue implantation and *in vivo* electrophysiology, we demonstrated the multiplexed electrophysiological recordings on the thermal-responsive mechanically adaptive polymer substrate. Then we aim to study the softening polymer based multimodal neural probe to monitor both neurotransmitter and electrophysiology as the same time. In this study, we target to sense serotonin, which is a key neurotransmitter along with electrophysiological recording.

We designed the multimodal neural probe on softening polymer SP2 (transition temperature 36.5 °C). The device was insulated by Parylene-C with three openings that will be in contact with the tissue, two on gold pads for electrophysiology and one on In₂O₃ ribbons for biosensing. Serpentine structures were used to increase the flexibility of metal and inorganic materials^[82-84].

Fig. 3.13 (a) illustrates the cross-sectional structure of the device. Following the microfabrication

process described in Section 3.3.3, we fabricated the FET sensor on polymer substrate, as shown in **Fig. 3.13 (b)**.

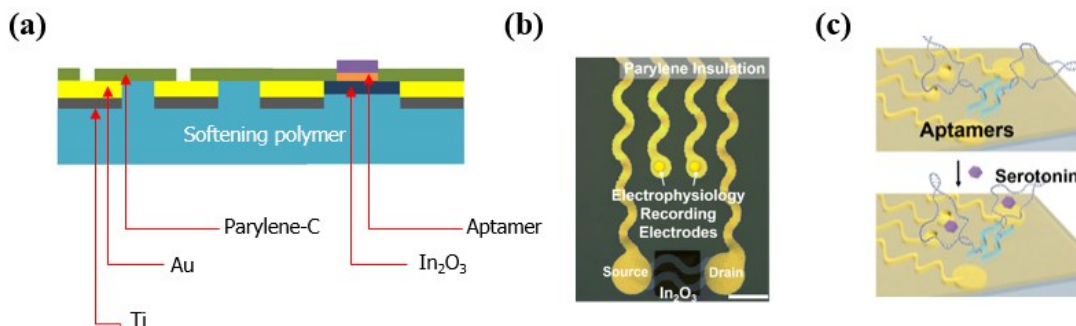


Figure 3.13 (a) Cross-sectional structure of the multimodal neural probe. **(b)** Optical microscopy image of the fabricated softening polymer based multimodal neural probe where two electrophysiological electrodes are on the top and an In₂O₃ nanoribbon field-effect transistor (FET) is on the bottom (Scale bar: 200 μ m). **(c)** Serotonin sensing mechanism: Conformation change after serotonin capture leads to the change of transconductance of In₂O₃.

Upon on serotonin capture, aptamers are hypothesized to move away from the semiconductor surface (In₂O₃). Serotonin aptamers used in this work are single-stranded DNA molecules with negatively charged backbones, and the movement induced by target binding will result in charge redistributions in the semiconductor channels (**Fig. 3.13 (c)**), where more negative charges will be presented. In₂O₃ is a *n*-type semiconductor, where an increase of channel conductance will be observed with more negative charges.

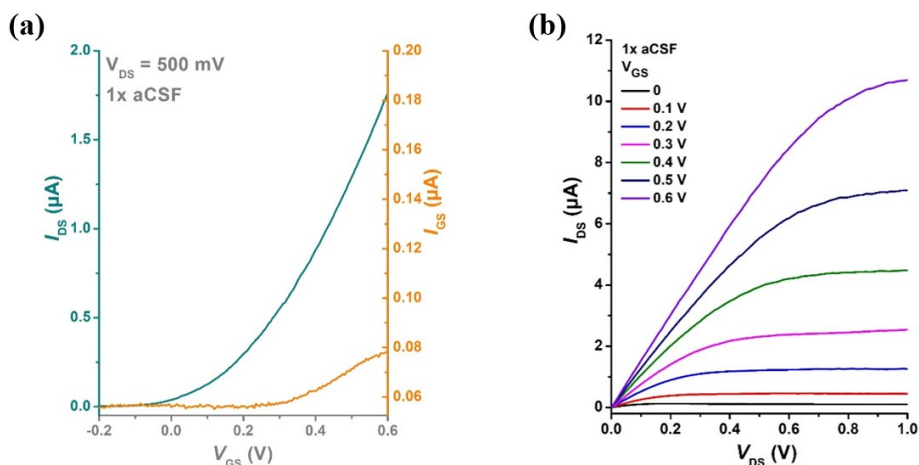


Figure 3.14 (a) Representative transfer characteristics of the In_2O_3 FETs in liquid gating configuration of aCSF. Left: source-drain current ($I_{\text{DS}}-V_{\text{GS}}$), right: source-gate current ($I_{\text{GS}}-V_{\text{GS}}$). The source-drain voltage V_{DS} was at constant of 500 mV. **(b)** Representative output characteristics of the In_2O_3 FETs in aCSF.

Representative transfer characteristics ($I_{\text{DS}}-V_{\text{GS}}$) and output characteristics ($I_{\text{DS}}-V_{\text{DS}}$) are shown in **Fig. 3.14 (a)** and **(b)**, respectively. In_2O_3 FETs were tested in artificial cerebrospinal fluid (aCSF)^[85, 86] and were gated by a Ag/AgCl electrode through the buffer solution. As shown in **Fig. 3.14 (a)**, the gate leakage ($I_{\text{GS}}-V_{\text{DS}}$) is more than one order of magnitude small compared with source-drain current. The calculated current on/off ratios in aCSF are $\sim 10^3$. The output characteristics indicates that the fabricated devices exhibited typical FET behavior with gate modulation. This validates the FET fabrication is successful on polymer substrate.

3.4.7 *In Vitro* and *Ex Vivo* Serotonin Sensing

To evaluate sensor reliability in a high-ionic-strength buffer that simulates the brain extra cellular fluid, the softening polymer-based serotonin sensor was first immersed in artificial cerebrospinal fluid (aCSF) for sensing testing.

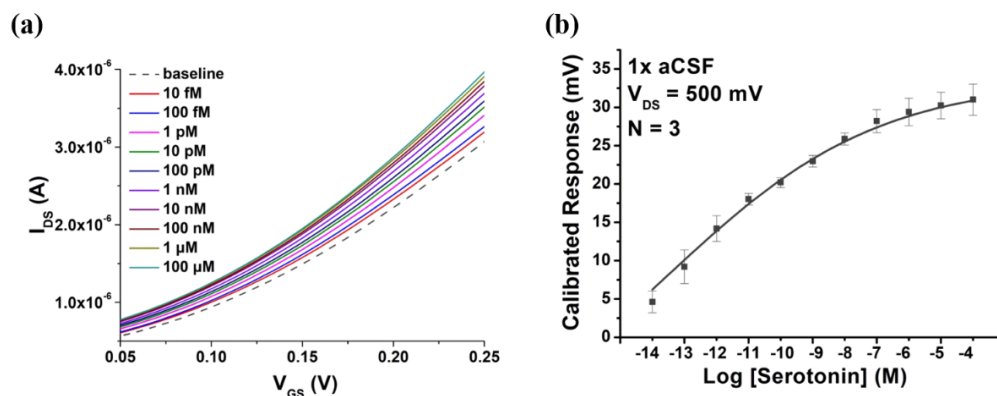


Figure 3.15 (a) Representative serotonin response curves in aCSF, where concentration-dependent increases were observed in source-drain currents while sweeping V_{GS} . (b) Calibrated responses of serotonin in aCSF from 10 fM to 100 μ M. N = 3. Error bars: standard error means.

Source-drain currents were monitored with gate voltage sweeping. As shown in Fig. 3.15 (a), the source-drain currents increased when serotonin was added to the solution, which is in consistence with the previous experimental results. Calibrated responses of gate voltage changes were calculated based on our previous work. Our sensors can detect serotonin from 10 fM to 100 μ M, which covers the physiological ranges of serotonin \sim 100 nM (Fig. 2g)^[85, 87]. The tests results show good sensitivity of the softening polymer-based sensor in aCSF.

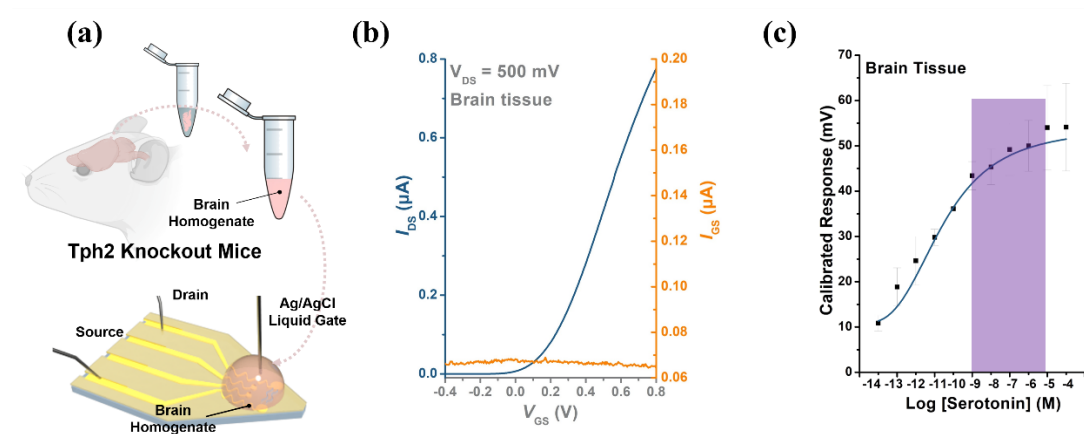


Figure 3.16 (a) Schematics of serotonin aptamer field-effect transistor (FET) biosensors *ex vivo* characterization in brain tissue. **(b)** Representative transfer characteristics of the In_2O_3 FET (green curve) and the gate-source voltage V_{GS} (orange curve). **(c)** Concentration-dependent responses for serotonin-aptamer functionalized FETs in homogenized brain tissue.

To evaluate sensing in an undiluted biological matrix, the serotonin sensing was also performed in homogenized brain tissue from mice lacking neuronal serotonin (i.e., *Tph2* null mice). The characterization is illustrated in **Fig. 3.16 (a)**. Representative transfer characteristics shown in **Fig. 3.16 (b)** indicates the stable FET performance in the homogenized tissue. Concentration-dependent responses from the polymer based neural probe was shown in **Fig. 3.16 (c)**. The sensing performance in tissue was stable and reproducible. The *ex vivo* results suggests that the serotonin sensor based on thermal-responsive, mechanically adaptive polymer substrate can be used for further *in vivo* study.

3.5 Conclusion

We demonstrated the softening polymer (SP2) with adaptive Young's modulus from $\sim 10^5$ kPa at room temperature to ~ 10 kPa at body temperature can be used as substrate for neural interfaces. A softening polymer based intracortical neural probe was fabricated and characterized. 85 μm -thick substrates ensure the successful insertion without buckling. Through *in vitro* characterization, the polymer can adapt to the tissue softness and reduce the strain induced by micromotion around the tip. Acute *in vivo* recording from the rat brain was done, showing the promise of the polymer as a smart substrate to build functional probes.

Furthermore, an aptamer-field-effect transistor (FET) neural probe was developed which can sense both serotonin signal and electrophysiological signals. The sensing performance was evaluated both *in vitro* and *ex vivo*.

The softening polymer could be a highly versatile platform technology that may yield all kinds of different probes. And the next-generation smart neural probe, which is adaptive, tissue-like soft, and multi-functional, can provide an unprecedented opportunity for combined behavioral studies with multimodal neural interrogation.

Chapter 4. Stretchable, Self-softening Epidural

Electrode Array

4.1 Introduction

4.1.1 Epidural Electrode Arrays for Spinal Cord Stimulation

Spinal cord injury (SCI) is a devastating and common neurologic disorder which can impact many areas of one's life.^[88, 89] Spinal cord electrical stimulation has been successfully applied to treat the SCI and restore the function of bladder^[90], bowel^[91], and locomotion^[26]. Among the spinal cord stimulations, epidural stimulation which involves the surgical implantation of a neurostimulator device on the posterior structures of the lumbar spinal cord can provide controlled, accurate excitation to the target neuron groups. Various implanted epidural electrode arrays have been developed and used to supply electrical currents to the electrodes^[79, 90] for spinal cord stimulation.

Till now, most of the epidural electrodes are fabricated on Polyimide or Parylene-C substrate, as these materials have been proved to be biocompatible and flexible. However, the stability of the interfaces created between the target neurons and the implanted electrodes suffers when large spinal deformation is present. Compared with brain, spinal cord has a larger deformation up to 20% when stretching and bending in humans as well as awake animals.^[92] The displacement and shear motion can lead to the foreign body reaction, or premature failure due to device breakage. Therefore, soft, compliant and stretchable epidural electrode arrays, capable of withstanding 20% strain to accommodate the spinal stretching, are needed to improve the tissue-electrode interface.

4.1.2 Stretchable Conductive Materials

Different stretchable conductive materials that can retain their electrical conduction at high strain have been studied. Metals, for example, have long been an obvious choice as a conventional conductor due to their high electrical conductivity. However, as most metals are as rigid as more than 100 GPa in Young's modulus, constructing them into stretchable traces can be challenging.

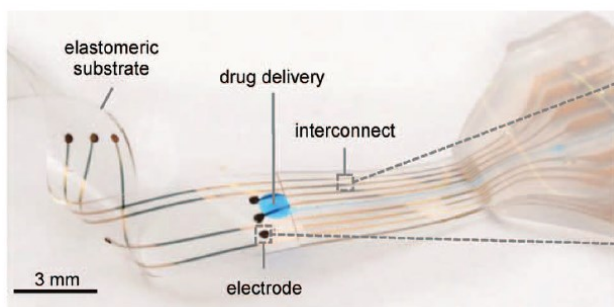


Figure 4.1 Electronic dura mater fabricated on PDMS using microcracked gold for stretchable neural interfaces (Photo citation [45]).

Creating of microcracked metal thin films on soft elastomer^[93] has been proved as an effective way to realize stretchability. Based on this method, Minev et. al fabricated a stretchable epidural electrode array using PDMS as the substrate.^[45] The device can maintain relatively stable electrical connection after cyclic applied strain up to 20%.

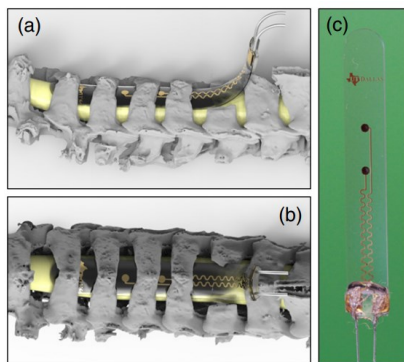


Figure 4.2 Chronic softening spinal cord stimulator with serpentine patterned electrodes (Photo citation: [94]).

Fabricating 2D serpentine patterns,^[95] or 3D buckled structures^[96] on stretchable substrates have also been utilized to realize stretchable conductors. Voit et. al developed a cervical spinal cord stimulator with serpentine electrodes on thiol-ene acrylate polymers. This softening polymer are stiff at room temperature and soften following implantation into the body.^[94] Less tissue deformation with the softening polymer was observed compared with Parylene-C probes.

Apart from metals, carbon nanotubes, conductive polymers (e.g. PEDOT:PSS), low melting point alloys (e.g. EGaln) have also been extensively investigated as building blocks for stretchable electronics. But for epidural electrodes applications, where low impedance and high resolution are required, these materials are not commonly adopted.

Recently, our group developed a (hydroxypropyl)methyl cellulose/ silver nanowires (AgNWs) ink that can achieve high-resolution patterns by stencil-based screen printing.^[97] After screen printing,

the homogeneous dispersion of AgNWs forms a high-density percolation network enabling the intrinsic stretchability of the conductive pattern.

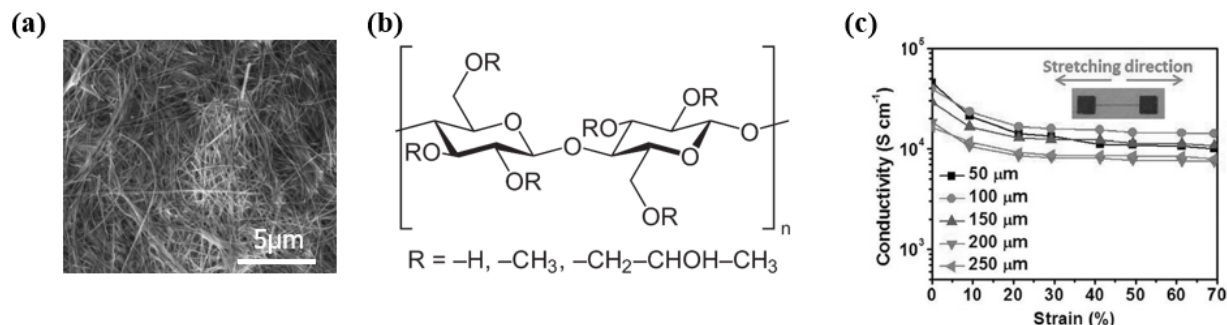


Figure 4.3 (a) SEM image of the silver nanowires. (b) Chemical structure of the (hydroxypropyl)methyl cellulose. (c) Conductivity change of screen-printed AgNW/PUA composite conductors as a function of tensile strain with various line widths (Photo citation: [97]).

The development of AgNWs ink presents a promising method to realize stretchable electronics through lithography-free, fully printing process with high resolution.

4.2 Proposed Methods

With the thermal-responsive, mechanically adaptive polymer SP2 (transition temperature 36.5 °C), we could potentially further reduce the mechanical mismatch to have a tissue-mimic, stretchable electronics for epidural electrode arrays. Therefore, we proposed to fabricate a self-softening, stretchable epidural electrode array based on stretchable silver nanowires and the softening polymer substrate.

To make sure the stiff Parylene-C insulation layer can also be stretched up to 20%, wrinkled Parylene-C structure was formed spontaneously on top of the substrate as a result of a simple pre stretching process. The concept of the electrode design was illustrated in **Fig. 4.4**.

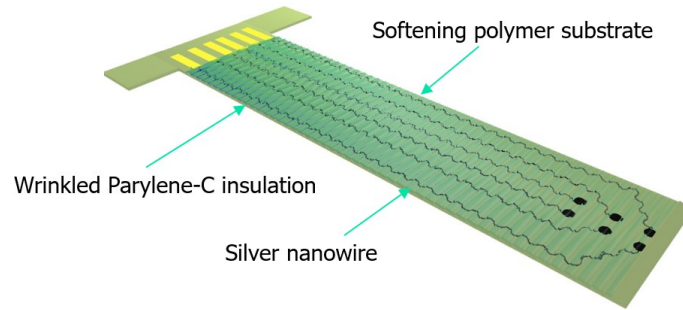


Figure 4.4 Schematic illustration of the stretchable epidural array based on silver nanowires and wrinkled Parylene-C.

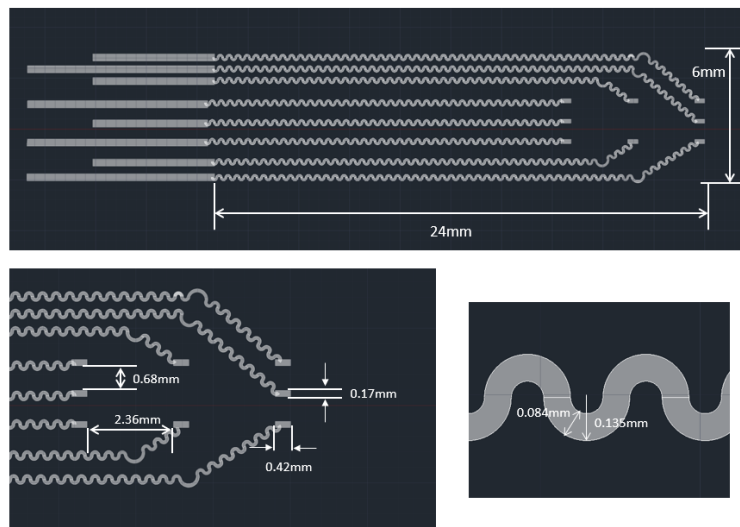


Figure 4.5 Geometry of the designed epidural electrode array.

The geometry of the designed electrode array (for the screen printing stencil as well) is shown in **Fig. 4.5**. It has 8 electrodes for the contact with neurons to delivery stimulations. Across the electrodes, serpentine pattern was designed to maximize the stretchability of the conductive traces. The end of the electrode array is connected to a zero-insertion force connector using Kapton tape as the stiffener.

4.3 Experiment Section

4.3.1 Materials

Urethane diacrylate CN9021, siliconized urethane acrylate oligomer CN990 were generously provided by Sartomer Company (Exton, PA). Hexadecyl acrylate (HA) was purchased from TCI America (Portland, OR). 2,2-Dimethoxy-2-phenylacetophenone, (hydroxypropyl)methyl cellulose (average Mn \approx 10 000), propylene glycol, and Platinum powders were obtained from Sigma-Aldrich (St. Louis, MO). AgNWs were purchased from Zhejiang Kechuang Advanced Materials Co., Ltd. The average diameter and length of the AgNWs are 25–35 nm and 15–25 μ m., Zonyl FS-300 was purchased from Fluka. Defoamer MO-2170 was requested from BASF. Fluor-surfactant FC-4430 was purchased from 3M. PDMS (Sylgard 184) was purchased from Dow Corning (Midland MI).

4.3.2 Fabrication of Epidural Electrode Array

The AgNWs ink preparation, screen printing methods and post treatment methods are similar as reported before.^[97] First, additive solution was obtained by mixing DI water, propylene glycol, (hydroxypropyl)methyl cellulose, Zonyl FS-300, and antifoaming agent at the weight ratio of

5:5:1:0.002:0.01. Then, the AgNWs solution (1 wt% in isopropyl alcohol), distilled water, and the additive solution were mixed at the weight ratio of 4:4:1 using VERTEX mixer at 1000 rpm for 1 h. Vacuum rotary evaporation was then used to dry the solution. DI water was added into the dried mixture and the ink was fully mixed before use.

Screen-printing was done using a squeegee pressing the conductive ink on HMI Model MSP-088 Bench Top Thick Film Screen Printer onto glass substrate. A stainless-steel screen mesh (400 mesh count, 0.0007 in. wire diameter, 0.0018 in. mesh opening, standard mesh tension, 22° mesh angle, 0.0008 in. emulsion thickness, emulsion is safe with water) ordered from Sefar Inc. was used as the stencil mask. The printed AgNW patterns were first annealed at 150 °C for 5 min to evaporate the solvent, followed by washing with ethanol and water mixture (1:20) for 5 min to remove part of the additives. Then, the AgNW pattern was heated to 150 °C again for 5 min, followed by washing with water for 5 min to remove most of the residual additives. Finally, the coating was annealed at 150 °C for 5 min to fuse the AgNW junctions, getting the final conductive AgNW pattern.

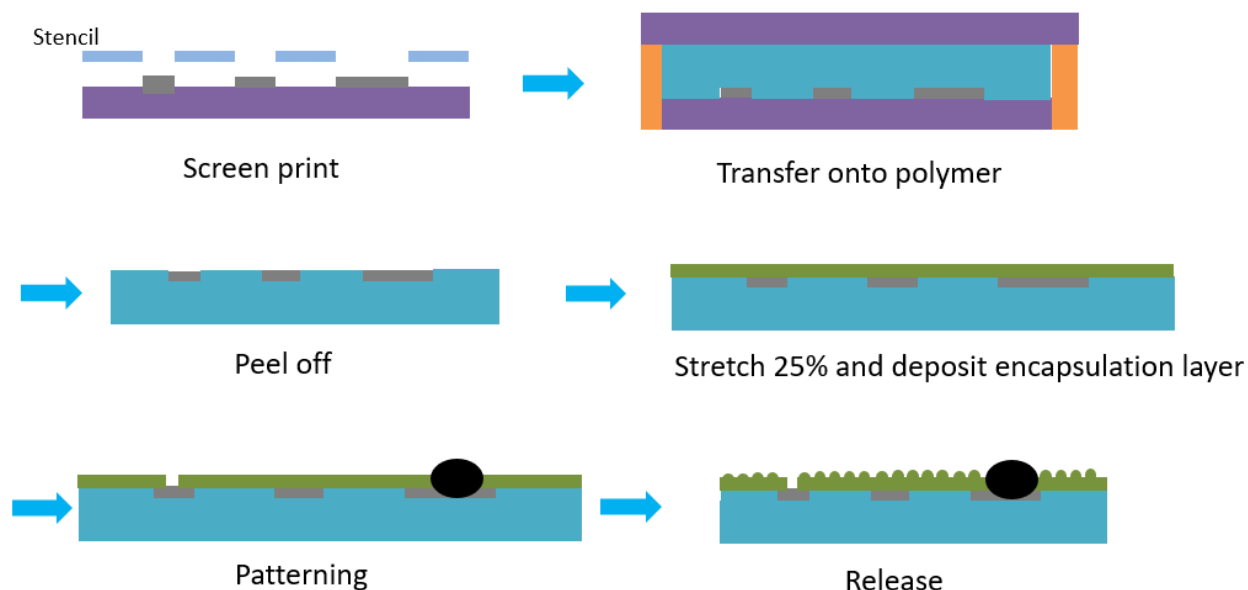


Figure 4.6 Fabrication process of the stretchable electrode array on softening polymer SP2.

The printed AgNW pattern printed on glass substrate were then spin-coated with a prepolymer solution CN990 with 1% DMPA at 4000rpm at 120 °C. Using the glass substrate as the bottom piece of a mold, the SP2 prepolymer solution was injected into the mold and cured similarly as the condition described in Chapter 3. After curing, the polymer was carefully peeled off and mounted on a linear state. The polymer film along with the stage was heated above 40 °C and pre-stretched 25% uniaxially. After cooling down the polymer below the transition temperature, the pre-strain was fixed.

600 nm of Parylene-C was then deposited in SCS Labcoter 2 Parylene Deposition System (PDS 2010, Specialty Coating Systems Inc., Indianapolis, IN) onto the pre-stretched SP2 substate, using PDMS as contact mask to protect the contact electrode area.

Soft platinum-silicone composite ink reported by Lacour et. al ^[45] was reproduced as the contact electrode for low-impedance, biocompatible electrical interconnect. Same method was used to formulate and print the 8 contact electrodes through shadow mask made of thin wax paper.

After the Pt/PDMS ink printing, the polymer film was put on the linear stage again and heated to 60 °C. The pre-strain was released until the polymer shrink back to the original shape. Wrinkled Parylene-C was self-formed on the softening polymer substrate.

4.4 Results and Discussion

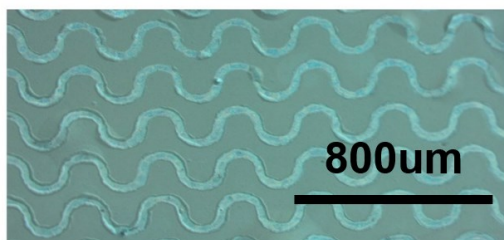


Figure 4.7 Microscopic image of a representative serpentine pattern with the AgNW ink.

The microscopic image shown in **Fig. 4.7** shows the screen-printing method and the AgNW ink can achieve resolution down to $\sim 50 \mu\text{m}$, satisfying the resolution requirements for epidural electrode array. The AgNW pattern with uniform line widths can be observed with clear edges. No voids or cracks were seen on the pattern.

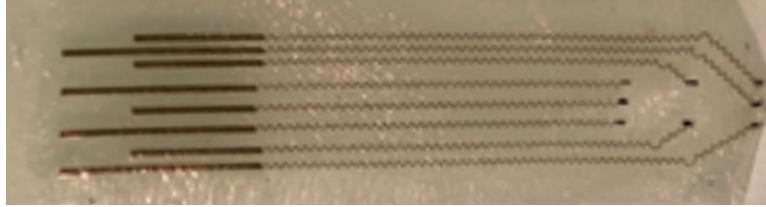


Figure 4.8 Image of the fabricated stretchable epidural electrode array with wrinkled Parylene-C encapsulation.

Parylene-C with the self-formed wrinkled structure can be seen from **Fig. 4.8**. The formation of wrinkles of a surface thin film on another dissimilar substrate has been studied before. Heating two layers with different coefficient of thermal expansion, releasing the pre-stretching of two layers with different Young's modulus or swelling of two layers with different swelling ratio can all lead to the wrinkle formation. In this case, the SP2 substrate is softer above transition temperature compared with Parylene-C. As the release of the pre-strain, the SP2 shrinks back and generates compressive force across the Parylene-C layer on top. When the force exceeds the critical value, wrinkles form.

Fig. 4.9 shows the Parylene-C wrinkle under microscope. The waves have a periodicity about 40 μm .

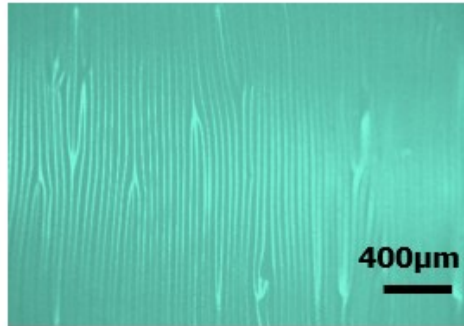


Figure 4.9 Microscopic image of the wrinkled Parylene-C in non-patterned area.

The screen printed AgNW pattern with $\sim 80 \mu\text{m}$ width has measured sheet resistance of $0.82 \pm 0.087 \Omega/\text{sq}$. The result is consistent with the previously reported value.^[97] The low sheet resistance ensures the stable connection as well as low impedance for the epidural electrode array.

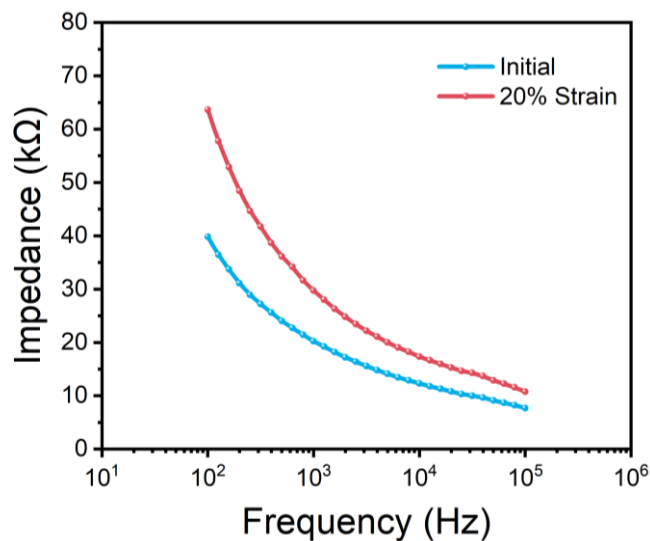


Figure 4.10 Electrical impedance measured in PBS before and after a uniaxial strain of 20%.

The electrical impedance measurements were performed in PBS at room temperature by using Princeton Applied Research Versastat 3 potentiostat. The test was set up in that the fabricated self-softening electrode served as a working electrode, Pt as counter electrode and an Ag/AgCl as reference electrode (saturated KCl-AgCl solution). A 10 mV RMS sinusoidal signal ranging from 100 kHz to 10 Hz was sent to the device. The impedance before and after 20 % uniaxial strain are shown in **Fig. 4.11** (n=8).

The electrodes composed of AgNW and Pt/PDMS have relatively low impedance with 20.2 k Ω at 1 kHz. After applying 20% uniaxial strain, the impedance increased to 29.7 k Ω at 1 kHz, which demonstrates the stability and reliability of the stretchable electrodes after stretching. This is attributed to the intrinsic stretchability of the AgNW network, as well as the serpentine pattern design which can reduce the plastic deformation in the AgNW and stabilize its electrical performance.

In addition, the polyurethane acrylate (CN990) acts as an interfacial layer between the softening polymer and the silver nanowires. The prepolymer solution can penetrate into the AgNW network so that the AgNWs are embedded into the polymer matrix. The embedding limits the slippage of AgNWs and formation of microcracks during stretching cycles. We have done comparison tests with and without the polyurethane acrylate interfacial layer. The samples without the interfacial layer cracked before reaching the 20% uniaxial strain.

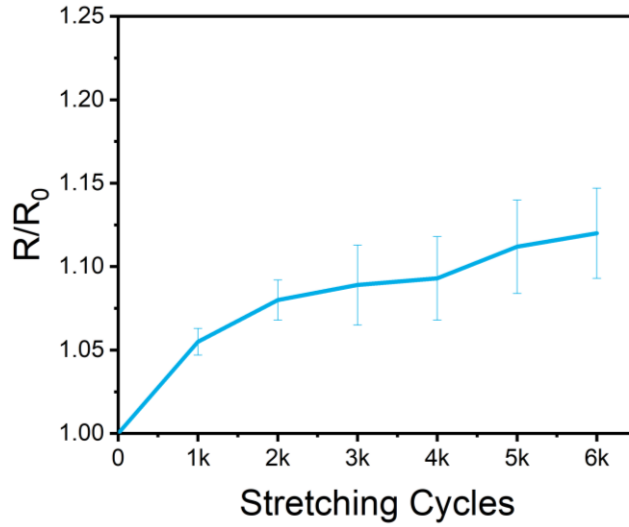


Figure 4.11 Relative resistance change of the silver nanowire conductive traces after cyclic 20% stretching (n=8).

To demonstrate the robustness of the stretchable, self-softening electrode, we perform the cyclic stretching test and measured the resistance increase from the AgNW lines and the impedance increase of the electrodes. The device was mounted on a linear stage on hot plate, heated above the body temperature range to ensure the fully softening of the SP2 substrate, and then stretched to 20% strain over 6000 cycles. As shown in Fig. 4.11, after 6000 cycles, the resistance of the AgNW pattern only increased less than 10% on average, indicating the great stability against strain induced fatigue. The impedance after stretching was also measured by same EIS methods described before. The impedance at 1 kHz increased less than 25%.

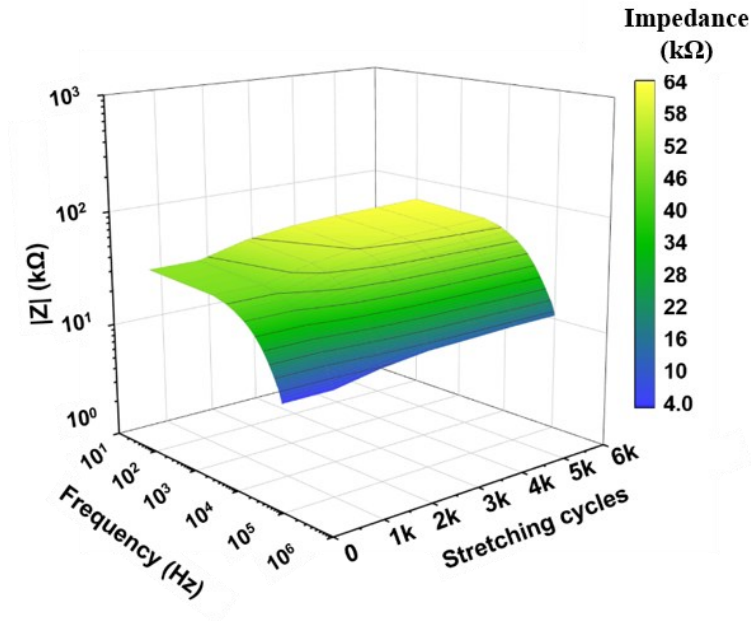


Figure 4.12 Impedance change of the stretchable, self-softening electrode array after cyclic 20% stretching (n=8).

The results show the great promise of the fabricated electrode array as body temperature softening stretchable neural interfaces to provide skin-like contact with the spinal cord. Further *in vivo* characterization is still ongoing to evaluate the performance of the epidural electrode array.

4.5 Conclusion

Based on the body temperature triggered softening polymer SP2, we designed a stretchable epidural electrode array. The stretchable conductive traces were screen printed silver nanowires transferred and embedded in the polymer substrate. The stretchability of rigid Parylene-C

encapsulation was achieved by creating wrinkled structure across of the film. The provides a universal method to endow rigid thin films a certain stretchability.

We measured the resistance change and impedance change after 6000 cycles stretching up to 20%. Both resistance from the AgNWs and the impedance from the whole device remain stable. The preliminary results validate the proposed methods to build the stretchable tissue-like epidural electrodes. Future works will be done to study the *in vivo* stimulation performance and stability in rats.

Chapter 5. A 2D Refreshable Braille Display Based on a Stiffness Variable Polymer and Pneumatic Actuation

5.1 Introduction

Vision impairment limits a person's ability to communicate, learn, work, and travel. It is estimated that there are 36 million blind people and additional 216.6 million severely visually impaired (SVI) patients around the world.^[98] In the United States alone, there are more than 1 million legally blind. Braille book has been the primary means for visually impaired individuals to read for over a century. Recently, with the development of refreshable Braille displays, a more flexible and efficient reading way has been provided. However, current Braille devices are generally bulky and expensive. A major reason behind is the limitation from the actuators used in the Braille devices.

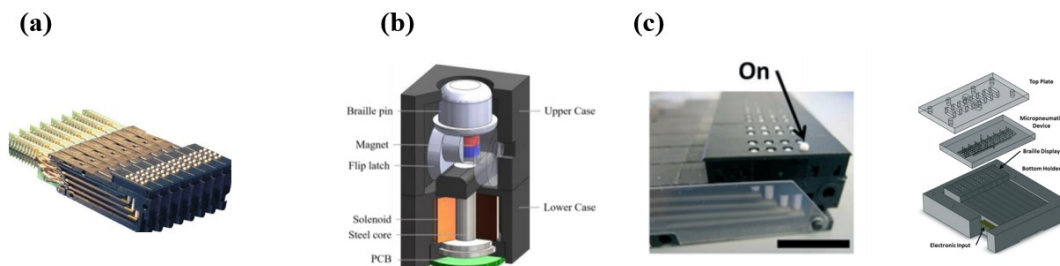


Figure 5.1 Representative actuators used in Braille displays. **(a)** Piezoelectric unimorph actuators used in P16 Braille cells (metec AG, Germany). **(b)** Electromagnetic actuators for Braille display (picture citation [99]). **(c)** Pneumatic actuators for Braille display (picture citation [100]).

Fig. 5.1 shows several representative actuators used in Braille displays. The most widely investigated is piezoelectric ceramic actuators. But devices based on piezoelectric bimorph or unimorph actuators^[101, 102] are typically bulky and expensive, due to the sophisticated mechanical elements and high operating voltage (100-300V).^[103] Shape memory alloy (SMA) coils actuators can also be used in as unimorph actuators, but shape memory alloy suffers from low portability and high working temperatures.^[104]

Electromagnetic actuators composed of the voice coil and permanent magnet were also investigated for Braille display.^[99, 104] The actuation controlled by electrical induced magnetic field change is a reliable and straightforward way to realize the Braille function. But the trade-off of EM devices is that to maintain the protruding force, the generated magnetic field needs to be held at a certain level. But if the magnetic field is too strong, it would negatively affect the surrounding pins. Therefore, it requires a well-designed structure to enable the actuation without interference. Other challenges with electromagnetic actuators include the heat dissipation and power consumption. For instance, constant current flow through the coils while maintaining the position of pins increases the overall power consumption.

Pneumatic actuation consisting of a pneumatic pump and built-in air channel is another way to achieve refreshable Braille display function. However, in order to access each dot independently, complex air channels need to be designed which adds more design complexity and volume occupied. Therefore, advances of actuator technology are needed for Braille displays.

We are living in an era of information explosion. The information we receive is not limited to text, but more multi-media based. The traditional actuator technologies used to display a single line of

braille alphabets are difficult to expand into 2D, to display images and videos. There is an urgent need to develop a 2D Braille display technology that enables multi-media communication. As 90% of the visually impaired people live in developing or underdeveloped countries,^[105] low cost is also an important factor to consider in developing the new braille technology.

5.2 Proposed Methods

We proposed a refreshable tactile display “PolyPad” based on stiffness variable polymer membrane and a miniature pneumatic pump. The large stiffness variation of the polymer membrane allows for large-strain deformation in the softened state by relatively low pneumatic pressures. The design eliminates the necessity to build complex air chain compared with common pneumatic actuator-based Braille displays. A 2D braille display panel (shown in **Fig. 5.2 (a)**) could be assembled using mostly off-the-shelf components.

The working principle is shown in **Fig. 5.2 (b)**. Each Braille dot can be individually controlled by heating and deforming the stiffness variable membrane with patterned Joule heating electrode. Then the corresponding pin will be lifted to interface with the end user. In this way, we can control each dot independently or control multiple dots at the same time without a complex air channel design. Upon cooling within 2 seconds, the dot position can be fixed due to polymer’s increased stiffness. No more power is needed for maintaining the “up” state of the pins. The rapid actuation and instant fixation enable high refresh rate, making it promising for large-scale Braille matrix applications.

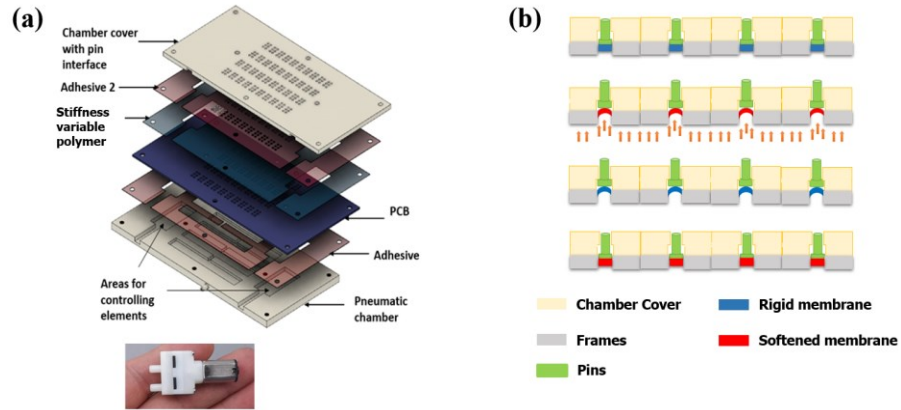


Figure 5.2 (a) Schematic illustration of the structure of the Braille PolyPad and **(b)** the cross-sectional working principle.

5.3 Experiment Section

The proposed prototype of PolyPad comprises a $6 \times 10 \times 4$ braille pixel dots matrix with an outer shell and printed circuit board (PCB) control system. Each dot has a 1.5 mm diameter with 2.5 mm dot center-to-center distance (designed according to the Braille standard). The device consists of three major parts: a PCB with chips for controlling the voltage output, a pneumatic system and a thin stiffness variable membrane that can be thermally controlled to soften locally. The pneumatic system consists of a pneumatic chamber and a miniature pump to provide pressurized air for actuation.

5.3.1 Materials

Urethane diacrylate (UDA) CN9021 was generously provided by Sartomer Company (Exton, PA). Stearyl acrylate, acrylic acid, benzophenone and 2,2-Dimethoxy-2-phenylacetophenone were purchased from Sigma-Aldrich (St. Louis, MO). P3-single walled carbon nanotube powder was purchased from Carbon Solution, Inc. All chemicals were used as received without further purification.

5.3.2 Stiffness Variable Polymers

Table 7 Formula of stiffness variable polymer membrane
(weight ratio)

Samples	SA	UDA	DMPA	BP	AA
BSEP	80	20	1	0.5	5

The materials enabling the controlled actuation include a stiffness variable polymer named “BSEP” (bistable electroactive polymers) and a Joule heating electrode. The formula of the polymer is shown in **Table 7**. **Fig. 5.3 (a)** shows the mechanical properties of a BSEP membrane measured on a dynamic mechanical analyzer (DMA). At room temperature, the BSEP possesses a modulus of 200 MPa and behaves as a rigid plastic capable of providing a high force output. Above its transition temperature, which is ~ 43 °C, the polymer becomes soft and stretchable, with its modulus decreasing to 0.2 MPa. In its soft state, the pneumatic pressure needed to displace 0.5mm

can be as low as 20kPa. It also has excellent stretchability with more than 300% elongation (**Fig. 5.3 (b)**).

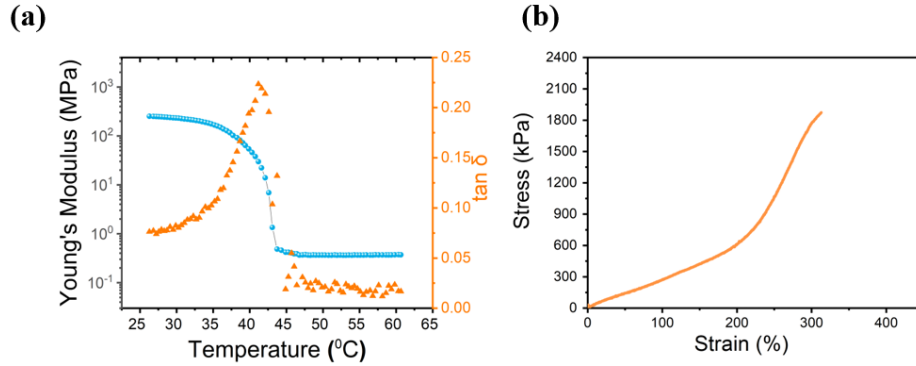


Figure 5.3 (a) Storage modulus and $\tan \delta$ versus temperature profile of the BSEP. **(b)** Stress strain curve of the BSEP membrane.

The transition temperature of the BSEP was designed to be only slightly above the room temperature, so that the required Joule heating energy for the stiffness transition can be reduced. Besides, the reversible phase transition allows for bistable actuation; the stiffened deformed membrane can keep the pins at the raised state without energy input.

5.3.3 Design of Joule Heating Electrode

To realize the controlled localized Joule heating with high precision, a matrix of a highly compliant single wall-carbon nanotubes (SW-CNT) electrodes are patterned into a serpentine shape on the surface of the BSEP film. The thermal stability, mechanical compliance, and chemical resistance of CNTs made it an ideal choice as the Joule heating electrode. The BSEP with the CNT electrode

is attached to the PCB and pneumatic chamber to ensure the chamber's airtightness. The rigid chamber covers, pneumatic pump and other components are then assembled for test.

The serpentine CNT Joule heating electrode is designed as shown in **Fig. 5.4 (a)**. In one cell, there are 6 small round areas for heating, and one bus line connected to the ground. The line thickness of the Joule heating electrode is 0.08 mm. The printed circuit board (PCB) was outsourced and customized according to the geometry of Braille spacing standard, and is shown in **Fig. 5.4 (b)**, and **(c)**. The control unit input voltage is 3.3V.

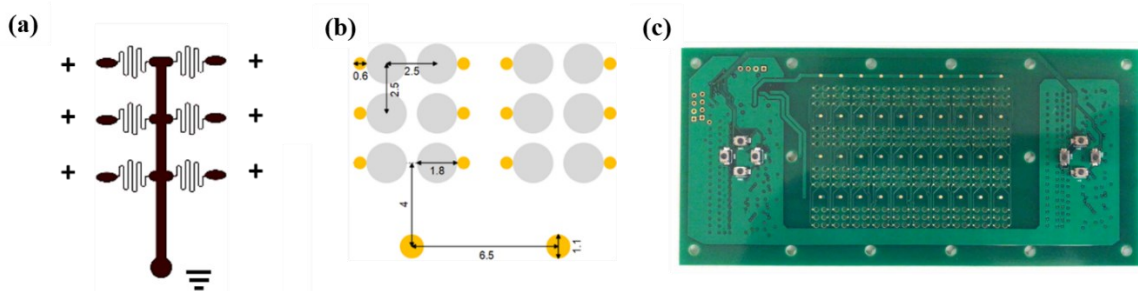


Figure 5.4 (a) Design of the serpentine carbon nanotube (CNT) electrode for localized Joule heating. **(b)** Design and dimension of the PCB top side for Joule heating control (Yellow: copper contact. Gray: Air channel). **(c)** Top view of the PCB.

5.3.4 Fabrication Process

The preparation of patterned CNT electrode on BSEP was briefly illustrated in **Fig. 5.5**. 5 mg of P3-single wall carbon nanotube powder was mixed with 1 mL of water and 20mL of IPA by sonication. Large aggregates were removed using a centrifuge at 8500rpm for 10min. The resulting

CNT supernatant was then spray coated onto clean glass substrate, patterned on an Epilog laser engraver.

A BSEP monomer solution was mixed and injected between a pair of glass slides on a hot plate with two strips of tape as spacers. The thickness of the liquid layer was defined by the thickness of the spacers. In the device assembly, 170 μ m thick spacers were used to fabricate the BSEP film. Next, the prepolymer was cured through a UV curing conveyor equipped with a Fusion 300S type “H” UV curing bulb for about 2 min. The cured film was gently peeled off the glass slide after it cooled down to room temperature. The patterned CNT was transferred to the BSEP film, as shown in Fig. 3(e). The sheet resistance of CNT could be adjusted by the spray coating amount of carbon nanotubes. Lower resistance leads to faster heating or lower driving voltage. However, as the thickness of the CNT increases, the risk of crack formation introduced by large deformation also increases.

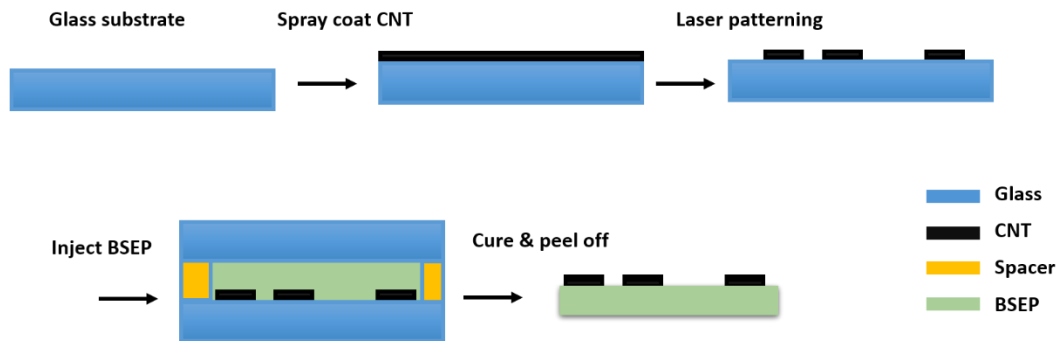


Figure 5.5 Fabrication process of the CNT pattern BSEP membrane.

After the CNT patterned BSEP membrane was prepared, it was laminated onto the PCB, with the CNT dots on the membrane and copper contact points on the PCB aligned with each other to form electrical connection in the z direction. The adhesion was enhanced by heating the BSEP with a heat gun for 30 seconds. The natural tackiness of the BSEP at its soft state ensures a good adhesion between the circuit board and the film. **Fig. 5.6** shows the image after the alignment.

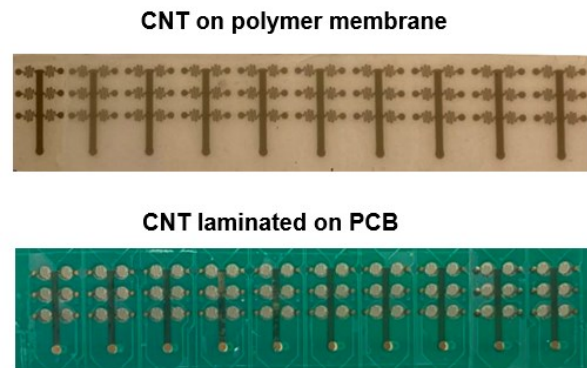


Figure 5.6 Image of CNT electrodes transferred onto the stiffness variable polymer membrane followed by lamination on to PCB.

5.4 Results and Discussion

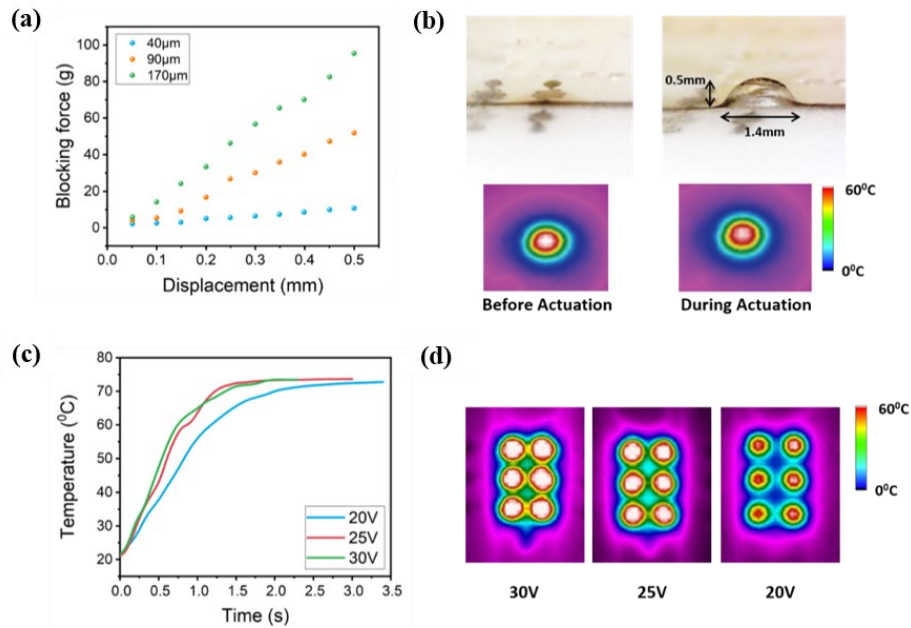


Figure 5.7 (a) Blocking force required to completely press down an actuated BSEP membranes of specified thickness. (b) Photo image and IR images of a dot before and during actuation. (c) Joule heating temperature ramp with different heating voltage. (d) IR image of a cell during Joule heating at specified voltages.

The blocking force of the Braille dots was measured by a force sensor. The films were all actuated to a raised height of 0.5 mm. Force was incrementally applied to press on the tip of the raised dots until the dots became flattened. The result is shown in **Fig. 5.7 (a)**. The measured blocking force at 0.5mm displacement is 95 grams for the BSEP membrane with thicknesses of 170 µm.^[106] The blocking force decreases with decreasing membrane thickness. The required blocking force in typical tactile devices is 15 g.^[107]

Fig. 5.7 (b) shows the IR image of a Braille dot during Joule heating before and during its actuation. The temperature in the center area is above 60 °C, ensuring the fully softening transition of the BSEP membrane. During the actuation at the height 0.5mm (which corresponds to area expansion of ~65% in the BSEP membrane), the temperature remains similar, showing that the CNT electrode was able to maintain its resistance at such large strains.

Different heating voltages were applied to study the heating speed of Braille dots of one cell, as the heating speed is closely related to the refresh rate of the device. The result is shown in **Fig. 5.7 (c)** and **(d)**. At 30 V, it takes ~0.5 s to reach the transition temperature of the BSEP membrane, while at 25 V it takes 0.6 s. Further lowering the heating voltage to 20 V slows the heating transition time to 0.7 s, but it can reduce the power consumption by ~54% per dot.

Braille pins placed on the BSEP membrane were used as the tactile interface. In the PolyPad prototype, the pins were 3D printed using Formlabs SLA 3D printer and then assembled into the chamber cover. The rapid manufacturing method enables fast modification of the Polypad prototyped. The chamber for air pump was sealed with pressure sensitive tape and tested for airtightness. The pneumatic actuation is achieved by a miniature pneumatic pump with the dimension of 32mm×8mm×18mm at 3 V.

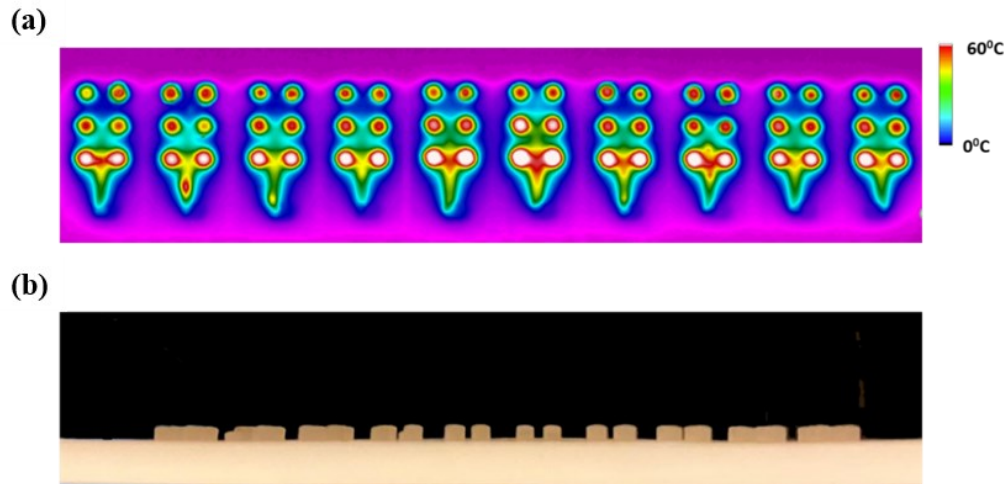


Figure 5.8 (a) IR image of one line Braille cells being Joule heated at 30 V. All dots are heated above the 45 °C transition temperature within 0.5 s. The power consumption at this voltage for heating 60 dots was estimated to be ~0.6 W. **(b)** The actuation of one line Braille cells of the PolyPad.

The first generation of the PolyPad design features 10×4 Braille cells. The preliminary experimental results have demonstrated the capability of using the stiffness variable polymer combined with a miniature pneumatic pump for the 2D Braille display. Through materials selection and electrodes design optimization, we addressed the challenge of CNT-based microelectrodes printed on BSEP membranes to realize efficient and fast Joule heating. The displacement and blocking force generated by the actuators are sufficient to satisfy the Braille standards. The proposed actuation mechanism and the fabrication process are expected to be scalable for high density tactile arrays.

5.5 Conclusion

We proposed a new 2D Braille display PolyPad based on the variable stiffness polymer BSEP coupled with pneumatic pumping. The BSEP membrane has reversible modulus change from 200 MPa to 0.2 MPa controlled by temperature. In preliminary prototype fabrication of the PolyPad, we successfully demonstrated the actuation mechanism and pixel addressability through the patterned Joule heating electrodes. Rapid actuation and height fixation of the Braille dots endow the PolyPad with a fast refresh rate for Braille display application. The heating and actuation uniformity among the Braille dots still need further improvement.

Work is ongoing to improve the performance of devices from three perspectives: 1. Enhance the Joule heating electrode reliability and robustness; 2. Improve airtightness of the device assembly such that the pneumatic pump may be further shrunk in size and power. 3. Add more features and controls to the device by designing PCB and encoders with more sophisticated functions, so that graphical images can be translated into 2D Braille dot patterns.

Chapter 6. Conclusion and Future Remarks

6.1 Conclusion

Stiffness variable materials, particularly stiffness variable polymers, have gained great attentions because of their potential to be used in smart structures, soft robotics and biomedical engineering. The previous chapters have reviewed several stiffness variable polymers and their potential applications. Research has been focusing on enlarging the Young's modulus change, and development of novel smart architectures and functional devices based on these materials.

In Chapter 2, we focus on a stiffness variable polymer system that composed of poly(n-alkyl acrylates) with crystallizable side chains. Fundamental study of the polymers was done to understand the effect of side chain length and other additives. The decrease of side chain length decreased transition temperature of the polymers to body temperature range. The removal of small-molecule crosslinker TMPTA from the previous polymer system enlarges the modulus change ratio. With this knowledge, a series of body temperature triggered stiffness variable polymers SP1 – SP4 were formulated, with transition temperature from 32 °C to 40 °C. The modulus change ratio was increased one more order of magnitude, and the transition range was narrowed to 3 °C for sharp transition. Biocompatibility study shows no cytotoxicity from these polymers, providing great promise to be used as biomaterials. For example, they can be potentially used as substrates thermal-responsive, mechanically adaptive neural interfaces, which are rigid before implantation and become soft after implantation.

In Chapter 3, based on these body-temperature triggered softening polymers, the application as neural interfaces were explored. An intracortical probe was designed and fabricated with the softening polymer substrate SP2. The feasibility of using microfabrication techniques to functionalize the mechanically adaptive polymer was proved. The resultant intracortical probe on the stiffness variable polymer can provide tissue-like contact with soft neural tissue and reduce the micromotion around the tip. The mechanical and electrical characterization was performed *in vitro*. Then, following *in vivo* electrophysiological recording experiment, the intracortical device paved ways for more functional devices based on this polymer.

Therefore, based on the same thermal-responsive, mechanically adaptive substrate, we further designed a multimodal neural probe that can sense both serotonin signal and electrophysiological signal. The working mechanism for serotonin sensing is an aptamer-based field-effect transistor (FET). The fabrication of the aptamer-FET sensor on the softening polymer was successful. *In vitro* and *ex vivo* characterization of the FET and the serotonin sensing demonstrated the versatility of the new polymer substrate for more multimodal sensors to be created.

In Chapter 4, the body-temperature triggered softening polymer was used as a substrate to achieve a stretchable epidural array for spinal cord use. The silver nanowire and the self-formed wrinkled Parylene-C enabled the 20% stretchability for the device. The electrical connection and property remain stable after stretching cycles. With this stretchable epidural array, the mechanical mismatch can be further reduced. And the tissue-like, wrap-around neural interfaces can be realized.

In Chapter 5, based on the stiffness variable polymer with higher transition temperature, we designed and prototyped a Braille display. Carbon nanotubes were micropatterned into Joule

heating electrode to trigger the softening of the stiffness variable polymer membrane, allowing for localized pneumatic actuation in the softened pin area. A miniature pump was used to pump up the softened membrane to enable a fast and controlled actuation. We realized the localized heating with the micropatterned electrodes on polymer substrates. And full-line actuation was demonstrated. This actuation technology provides a good way to create low-cost 2D refreshable Braille displays.

In summary, this dissertation studies novel stiffness variable polymers and explored building microelectronic sensors and actuators on these polymers. The stiffness variable polymers have been proved to be a versatile platform for more smart functional devices.

6.2 Outlook and Future Works

This dissertation has studied the thermal-responsive poly(n-alkyl acrylates) as stiffness variable polymers and demonstrated several microelectronic sensors and actuators based on these materials. Especially, the body temperature triggered softening polymers have been used to build different microelectronic arrays and sensors for the next-generation neural interfaces. However, further development is still needed for the stiffness variable polymers in two aspects: 1. Materials improvement and 2. Device developments.

In terms of the materials, the current stiffness variable polymers have achieved kPa, tissue-mimic softness, but they cannot reach high rigidity >1 GPa. A higher Young's modulus will benefit the implantable neural probes in decreasing the footprint after insertion. To achieve this, the polymer nanocomposites can be considered with incorporated second phase for reinforcement. The second

phase should also be responsive to external stimuli so that its softness will not be sacrificed. Meanwhile, the tensile stress of the polymer can be further enhanced. Higher tensile stress will promote the protection of the polymer matrix and the microelectronics in larger deformation. This will benefit especially in chronic neural interfaces.

The stiffness variable polymers can be engineered to responds to other stimulus as well: pH, moisture, DNA, pressure, etc. How can a trace amount of stimulus trigger a large modulus change? Designing the mechanism will be interesting.

From the device perspective, non-tethered, wireless neural stimulators or probes have been developed on different substrates. Wireless, bidirectional communication between the implanted device and the external machine will greatly facilitate the applications of neural interfaces to benefit more people. Opportunities are presented to integrate those wireless devices onto stiffness variable polymers to realize more intimate contact.

In addition, non-invasive devices are safer to humans. With the devices built on the skin-temperature triggered softening polymers, we could build more epidermal sensors to monitor physiological index like blood pressure. The skin-like and imperceptible electronics will be a fascinating next-generation human-machine interface.

Currently, the microelectronics with high circuits density are all built with photolithography method. The fabrication is an expensive and complicated process, thus limiting the ease of access. If future smart devices are targeting for everyday use, cost-effective materials and manufacturing method need to be developed. New stiffness variable polymers can be developed as a disposable

substrate of tattoo electronics. Printing circuits may also replace part of the photolithography steps for easier, cleaner and more cost-effective process.

In summary, the future for smart polymers and smart devices is bright, and it deserves more efforts from academia and industry.

Reference

- [1] Q. Pei, *Soft Robotics* **2016**, 3, 1.
- [2] J. R. Capadona, K. Shanmuganathan, D. J. Tyler, S. J. Rowan and C. Weder, *Science* **2008**, 319, 1370-1374.
- [3] A. Firouzeh and J. Paik, *Smart Materials and Structures* **2017**, 26, 055035.
- [4] G. Pang, G. Yang, W. Heng, Z. Ye, X. Huang, H.-Y. Yang and Z. Pang, *IEEE Transactions on Industrial Electronics* **2020**, 68, 3303-3314.
- [5] Q. Ai, P. M. Weaver and M. Azarpeyvand, *Journal of Intelligent Material Systems and Structures* **2018**, 29, 669-683.
- [6] G. Mcknight, R. Doty, A. Keefe, G. Herrera and C. Henry, *Journal of Intelligent Material Systems and Structures* **2010**, 21, 1783-1793.
- [7] J. Shintake, B. Schubert, S. Rosset, H. Shea and D. Floreano, *2015 IEEE/RSJ International Conference on Intelligent Robots and Systems (IROS)* **2015**, pp. 1097-1102.
- [8] C. English and D. Russell, *Mechanism and Machine Theory* **1999**, 34, 7-25.
- [9] C. Chautems, A. Tonazzini, D. Floreano and B. J. Nelson, *2017 IEEE/RSJ International Conference on Intelligent Robots and Systems (IROS)* **2017**, pp. 181-186.
- [10] I. De Falco, M. Cianchetti and A. Menciassi, *Bioinspiration & Biomimetics* **2017**, 12, 056008.
- [11] Y. Yang, Y. Chen, Y. Li, M. Z. Chen and Y. Wei, *Soft Robotics* **2017**, 4, 147-162.
- [12] T. Defize, J.-M. Thomassin, H. Ottevaere, C. d. Malherbe, G. Eppe, R. Jellali, M. I. Alexandre, C. Jérôme and R. I. Riva, *Macromolecules* **2018**, 52, 444-456.

- [13] X. Qi, X. Yao, S. Deng, T. Zhou and Q. Fu, *Journal of Materials Chemistry A* **2014**, *2*, 2240-2249.
- [14] K. Gall, C. M. Yakacki, Y. Liu, R. Shandas, N. Willett and K. S. Anseth, *Journal of Biomedical Materials Research Part A* **2005**, *73*, 339-348.
- [15] N. Amalia, E. Yuliza, D. O. Margaretta, F. D. Utami, N. Surtiyeni, S. Viridi and M. Abdullah, *AIP Advances* **2018**, *8*, 115201.
- [16] J. D. Menczel and R. B. Prime, *Thermal Analysis of Polymers: Fundamentals and Applications*, John Wiley & Sons, **2009**.
- [17] B. Yang, W. M. Huang, C. Li and J. H. Chor, *European Polymer Journal* **2005**, *41*, 1123-1128.
- [18] T. Ware, D. Simon, D. E. Arreaga-Salas, J. Reeder, R. Rennaker, E. W. Keefer and W. Voit, *Advanced Functional Materials* **2012**, *22*, 3470-3479.
- [19] Y. Meng, J. Jiang and M. Anthamatten, *Journal of Polymer Science Part B: Polymer Physics* **2016**, *54*, 1397-1404.
- [20] W. F. Daniel, G. Xie, M. Vatankhah Varnoosfaderani, J. Burdyska, Q. Li, D. Nykypanchuk, O. Gang, K. Matyjaszewski and S. S. Sheiko, *Macromolecules* **2017**, *50*, 2103-2111.
- [21] Z. Ren, W. Hu, C. Liu, S. Li, X. Niu and Q. Pei, *Macromolecules* **2016**, *49*, 134-140.
- [22] W. Hu, Z. Ren, J. Li, E. Askounis, Z. Xie and Q. Pei, *Advanced Functional Materials* **2015**, *25*, 4827-4836.
- [23] S. Harkema, Y. Gerasimenko, J. Hodes, J. Burdick, C. Angeli, Y. Chen, C. Ferreira, A. Willhite, E. Rejc, R. G. Grossman and V. R. Edgerton, *Lancet* **2011**, *377*, 1938-1947.

- [24] T. J. Oxley, N. L. Opie, S. E. John, G. S. Rind, S. M. Ronayne, T. L. Wheeler, J. W. Judy, A. J. McDonald, A. Dornom, T. J. Lovell, C. Steward, D. J. Garrett, B. A. Moffat, E. H. Lui, N. Yassi, B. C. Campbell, Y. T. Wong, K. E. Fox, E. S. Nurse, I. E. Bennett, S. H. Bauquier, K. A. Liyanage, N. R. van der Nagel, P. Perucca, A. Ahnood, K. P. Gill, B. Yan, L. Churilov, C. R. French, P. M. Desmond, M. K. Horne, L. Kiers, S. Prawer, S. M. Davis, A. N. Burkitt, P. J. Mitchell, D. B. Grayden, C. N. May and T. J. O'Brien, *Nature Biotechnology* **2016**, *34*, 320.
- [25] M. Capogrosso, T. Milekovic, D. Borton, F. Wagner, E. M. Moraud, J.-B. Mignardot, N. Buse, J. Gandar, Q. Barraud, D. Xing, E. Rey, S. Duis, Y. Jianzhong, W. K. Ko, Q. Li, P. Detemple, T. Denison, S. Micera, E. Bezdard, J. Bloch and G. Courtine, *Nature* **2016**, *539*, 284.
- [26] P. Gad, J. Choe, M. S. Nandra, H. Zhong, R. R. Roy, Y.-C. Tai and V. R. Edgerton, *Journal of Neuroengineering and Rehabilitation* **2013**, *10*, 1-18.
- [27] A. Pongracz, Z. Fekete, G. Márton, Z. Bérces, I. Ulbert and P. Fürjes, *Sensors and Actuators B: Chemical* **2013**, *189*, 97-105.
- [28] N. Fatima, A. Shuaib and M. Saqqur, *Clinical Neurology and Neurosurgery* **2020**, *196*, 106069.
- [29] V. Pikov, D. B. McCreery and M. Han, *Journal of Neural Engineering* **2020**, *17*, 065004.
- [30] J. J. Jun, N. A. Steinmetz, J. H. Siegle, D. J. Denman, M. Bauza, B. Barbarits, A. K. Lee, C. A. Anastassiou, A. Andrei, C. Aydin, M. Barbic, T. J. Blanche, V. Bonin, J. Couto, B. Dutta, S. L. Gratiy, D. A. Gutnisky, M. Hausser, B. Karsh, P. Ledochowitsch, C. M. Lopez, C. Mitelut, S. Musa, M. Okun, M. Pachitariu, J. Putzeys, P. D. Rich, C. Rossant, W. L. Sun, K. Svoboda, M. Carandini, K. D. Harris, C. Koch, J. O'Keefe and T. D. Harris, *Nature* **2017**, *551*, 232–236.

- [31] J. F. Lin, H. P. Scott, R. A. Fischer, Y. Y. Chang, I. Kantor and V. B. Prakapenka, *Geophysical Research Letters* **2009**, *36*, L06306.
- [32] C. Xie, J. Liu, T.-M. Fu, X. Dai, W. Zhou and C. M. Lieber, *Nature Materials* **2015**, *14*, 1286.
- [33] G. Hong, R. D. Viveros, T. J. Zwang, X. Yang and C. M. Lieber, *Biochemistry* **2018**, *57*, 3995-4004.
- [34] J. C. Barrese, N. Rao, K. Paroo, C. Triebwasser, C. Vargas-Irwin, L. Franquemont and J. P. Donoghue, *Journal of Neural Engineering* **2013**, *10*, 066014.
- [35] R. Chen, A. Canales and P. Anikeeva, *Nature Reviews Materials* **2017**, *2*, 16093.
- [36] A. B. Schwartz, *The Annual Review of Neuroscience* **2004**, *27*, 487–507.
- [37] T. D. Y. Kozai, A. L. Vazquez, C. L. Weaver, S.-G. Kim and X. T. Cui, *Journal of Neural Engineering* **2012**, *9*, 066001.
- [38] L. Bollmann, D. E. Koser, R. Shahapure, H. O. Gautier, G. A. Holzapfel, G. Scarcelli, M. C. Gather, E. Ulbricht and K. Franze, *Frontiers in Cellular Neuroscience* **2015**, *9*, 363.
- [39] J. W. Salatino, K. A. Ludwig, T. D. Kozai and E. K. Purcell, *Nature Biomedical Engineering* **2017**, *1*, 862.
- [40] R. Feiner and T. Dvir, *Nature Reviews Materials* **2017**, *3*, 17076.
- [41] H. S. Sohal, A. Jackson, R. Jackson, G. J. Clowry, K. Vassilevski, A. O’Neill and S. N. Baker, *Frontiers in Neuroengineering* **2014**, *7*, 10.
- [42] L. Luan, X. Wei, Z. Zhao, J. J. Siegel, O. Potnis, C. A. Tuppen, S. Lin, S. Kazmi, R. A. Fowler, S. Holloway, A. K. Dunn, R. A. Chitwood and C. Xie, *Science Advances* **2017**, *3*, e1601966.

- [43] X. Wei, L. Luan, Z. Zhao, X. Li, H. Zhu, O. Potnis and C. Xie, *Advanced Science* **2018**, *5*, 1700625.
- [44] S. P. Lacour, S. Benmerah, E. Tarte, J. FitzGerald, J. Serra, S. McMahon, J. Fawcett, O. Graudejus, Z. Yu and B. Morrison, *Medical & Biological Engineering & Computing* **2010**, *48*, 945–954.
- [45] I. R. Mineev, P. Musienko, A. Hirsch, Q. Barraud, N. Wenger, E. M. Moraud, J. Gandar, M. Capogrosso, T. Milekovic, L. Asboth, R. F. Torres, N. Vachicouras, Q. Liu, N. Pavlova, S. Duis, A. Larmagnac, J. Voros, S. Micera, Z. Suo, G. Courtine and S. P. Lacour, *Science* **2015**, *347*, 159–163.
- [46] Y. Lu, D. Wang, T. Li, X. Zhao, Y. Cao, H. Yang and Y. Y. Duan, *Biomaterials* **2009**, *30*, 4143–4151.
- [47] U. A. Aregueta-Robles, A. J. Woolley, L. A. Poole-Warren, N. H. Lovell and R. A. Green, *Frontiers in Neuroengineering* **2014**, *7*, 15.
- [48] Y. Liu, J. Liu, S. Chen, T. Lei, Y. Kim, S. Niu, H. Wang, X. Wang, A. M. Foudeh, J. B. Tok and Z. Bao, *Nature Biomedical Engineering* **2019**, *3*, 58–68.
- [49] A. J. Shoffstall, S. Srinivasan, M. Willis, A. M. Stiller, M. Ecker, W. E. Voit, J. J. Pancrazio and J. R. Capadona, *Scientific Reports* **2018**, *8*, 122.
- [50] A. Lecomte, V. Castagnola, E. Descamps, L. Dahan, M. Blatché, T. Dinis, E. Leclerc, C. Egles and C. Bergaud, *Journal of Micromechanics and Microengineering* **2015**, *25*, 125003.
- [51] L. W. Tien, F. Wu, M. D. Tang-Schomer, E. Yoon, F. G. Omenetto and D. L. Kaplan, *Advanced Functional Materials* **2013**, *23*, 3185–3193.

- [52] T. Kozai, T. Marzullo, F. Hooi, N. Langhals, A. Majewska, E. Brown and D. Kipke, *Journal of Neural Engineering* **2010**, 7, 046011.
- [53] J. Harris, A. E. Hess, S. J. Rowan, C. Weder, C. Zorman, D. Tyler and J. R. Capadona, *Journal of Neural Engineering* **2011**, 8, 046010.
- [54] J. Harris, J. Capadona, R. Miller, B. Healy, K. Shanmuganathan, S. Rowan, C. Weder and D. Tyler, *Journal of Neural Engineering* **2011**, 8, 066011.
- [55] T. Ware, D. Simon, C. Liu, T. Musa, S. Vasudevan, A. Sloan, E. W. Keefer, R. L. Rennaker and W. Voit, *Journal of Biomedical Materials Research Part B: Applied Biomaterials* **2014**, 102, 1-11.
- [56] A. Lendlein and R. Langer, *Science* **2002**, 296, 1673-1676.
- [57] M. Ahmad, J. Luo, B. Xu, H. Purnawali, P. J. King, P. R. Chalker, Y. Fu, W. Huang and M. Mirafteb, *Macromolecular Chemistry and Physics* **2011**, 212, 592-602.
- [58] Y. Shibasaki and K. Fukuda, *Journal of Polymer Science: Polymer Chemistry Edition* **1980**, 18, 2437-2449.
- [59] T. Hirabayashi, T. Kikuta, K. Kasabou and K. Yokota, *Polymer Journal* **1988**, 20, 693-698.
- [60] W. F. Daniel, J. Burdyńska, M. Vatankhah-Varnoosfaderani, K. Matyjaszewski, J. Paturej, M. Rubinstein, A. V. Dobrynin and S. S. Sheiko, *Nature Materials* **2016**, 15, 183.
- [61] J. Lin, J. Wu, Z. Yang and M. Pu, *Macromolecular Rapid Communications* **2001**, 22, 422-424.
- [62] K. O'Leary and D. Paul, *Polymer* **2006**, 47, 1226-1244.
- [63] N. Plate, V. Shibaev, B. Petrukhin, Y. A. Zubov and V. Kargin, *Journal of Polymer Science Part A: Polymer Chemistry* **1971**, 9, 2291-2298.

- [64] F. Gackière and L. Vinay, *Frontiers in Neural Circuits* **2014**, *8*, 102.
- [65] F. E. Perrin and H. N. Noristani, *Experimental Neurology* **2019**, *318*, 174-191.
- [66] A. M. Andrews, *ACS Chem Neurosci* **2013**, *4*, 645.
- [67] A. P. Alivisatos, M. Chun, G. M. Church, K. Deisseroth, J. P. Donoghue, R. J. Greenspan, P. L. McEuen, M. L. Roukes, T. J. Sejnowski, P. S. Weiss and R. Yuste, *Science* **2013**, *339*, 1284–1285.
- [68] A. P. Alivisatos, A. M. Andrews, E. S. Boyden, M. Chun, G. M. Church, K. Deisseroth, J. P. Donoghue, S. E. Fraser, J. Lippincott-Schwartz, L. L. Looger, S. Masmanidis, P. L. McEuen, A. V. Nurmikko, H. Park, D. S. Peterka, C. Reid, M. L. Roukes, A. Scherer, M. Schnitzer, T. J. Sejnowski, K. L. Shepard, D. Tsao, G. Turrigiano, P. S. Weiss, C. Xu, R. Yuste and X. Zhuang, *ACS Nano* **2013**, *7*, 1850–1866.
- [69] A. M. Andrews, A. Schepartz, J. V. Sweedler and P. S. Weiss, *Journal of the American Chemical Society* **2014**, *136*, 1–2.
- [70] J. Kim, Y. S. Rim, H. Chen, H. H. Cao, N. Nakatsuka, H. L. Hinton, C. Zhao, A. M. Andrews, Y. Yang and P. S. Weiss, *ACS Nano* **2015**, *9*, 4572–4582.
- [71] N. Nakatsuka, K. A. Yang, J. M. Abendroth, K. M. Cheung, X. Xu, H. Yang, C. Zhao, B. Zhu, Y. S. Rim, Y. Yang, P. S. Weiss, M. N. Stojanovic and A. M. Andrews, *Science* **2018**, *362*, 319–324.
- [72] K. M. Cheung, K. A. Yang, N. Nakatsuka, C. Zhao, M. Ye, M. E. Jung, H. Yang, P. S. Weiss, M. N. Stojanovic and A. M. Andrews, *ACS Sens* **2019**, *4*, 3308–3317.
- [73] Q. Liu, C. Zhao, M. Chen, Y. Liu, Z. Zhao, F. Wu, Z. Li, P. S. Weiss, A. M. Andrews and C. Zhou, *iScience* **2020**, *23*, 101469.

- [74] K. M. Cheung, J. M. Abendroth, N. Nakatsuka, B. Zhu, Y. Yang, A. M. Andrews and P. S. Weiss, *Nano Letters* **2020**, *20*, 5982–5990.
- [75] R. Pomfret, G. Miranpuri and K. Sillay, *Annals of Neurosciences* **2013**, *20*, 118.
- [76] V. Normand, D. L. Lootens, E. Amici, K. P. Plucknett and P. Aymard, *Biomacromolecules* **2000**, *1*, 730-738.
- [77] L. Karumbaiah, S. E. Norman, N. B. Rajan, S. Anand, T. Saxena, M. Betancur, R. Patkar and R. V. Bellamkonda, *Biomaterials* **2012**, *33*, 5983-5996.
- [78] K. C. Spencer, J. C. Sy, K. B. Ramadi, A. M. Graybiel, R. Langer and M. J. Cima, *Scientific Reports* **2017**, *7*, 1-16.
- [79] P. Gad, I. Lavrov, P. Shah, H. Zhong, R. R. Roy, V. R. Edgerton and Y. Gerasimenko, *Journal of Neurophysiology* **2013**, *110*, 1311-1322.
- [80] I. Lavrov, Y. P. Gerasimenko, R. M. Ichiyama, G. Courtine, H. Zhong, R. R. Roy and V. R. Edgerton, *Journal of Neurophysiology* **2006**, *96*, 1699-1710.
- [81] I. Lavrov, C. J. Dy, A. J. Fong, Y. Gerasimenko, G. Courtine, H. Zhong, R. R. Roy and V. R. Edgerton, *Journal of Neuroscience* **2008**, *28*, 6022-6029.
- [82] Y. Zhang, S. Xu, H. Fu, J. Lee, J. Su, K.-C. Hwang, J. A. Rogers and Y. Huang, *Soft Matter* **2013**, *9*, 8062-8070.
- [83] Y. Zhang, S. Wang, X. Li, J. A. Fan, S. Xu, Y. M. Song, K. J. Choi, W. H. Yeo, W. Lee and S. N. Nazaar, *Advanced Functional Materials* **2014**, *24*, 2028-2037.
- [84] K. Li, X. Cheng, F. Zhu, L. Li, Z. Xie, H. Luan, Z. Wang, Z. Ji, H. Wang and F. Liu, *Advanced Functional Materials* **2019**, *29*, 1806630.

- [85] H. Yang, M. M. Sampson, D. Senturk and A. M. Andrews, *ACS Chemical Neuroscience* **2015**, *6*, 1487–1501.
- [86] C. Zhao, Q. Liu, K. M. Cheung, W. Liu, Q. Yang, X. Xu, T. Man, P. S. Weiss, C. Zhou and A. M. Andrews, *ACS Nano* **2021**, *15*, 904–915.
- [87] H. Yang, A. B. Thompson, B. J. McIntosh, S. C. Altieri and A. M. Andrews, *ACS Chemical Neuroscience* **2013**, *4*, 790–798.
- [88] R. J. Dumont, D. O. Okonkwo, S. Verma, R. J. Hurlbert, P. T. Boulos, D. B. Ellegala and A. S. Dumont, *Clinical Neuropharmacology* **2001**, *24*, 254-264.
- [89] L. A. Simpson, J. J. Eng, J. T. Hsieh, Wolfe and D. L. the Spinal Cord Injury Rehabilitation Evidence Research Team, *Journal of Neurotrauma* **2012**, *29*, 1548-1555.
- [90] P. N. Gad, R. R. Roy, H. Zhong, D. C. Lu, Y. P. Gerasimenko and V. R. Edgerton, *PloS one* **2014**, *9*, e108184.
- [91] M. Walter, A. H. Lee, A. Kavanagh, A. A. Phillips and A. V. Krassioukov, *Frontiers in Physiology* **2018**, *9*, 1816.
- [92] B. Ji, Z. Xie, W. Hong, C. Jiang, Z. Guo, L. Wang, X. Wang, B. Yang and J. Liu, *Journal of Materiomics* **2020**, *6*, 330-338.
- [93] I. M. Graz, D. P. Cotton and S. P. Lacour, *Applied Physics Letters* **2009**, *94*, 071902.
- [94] A. Garcia-Sandoval, A. Pal, A. M. Mishra, S. Sherman, A. R. Parikh, A. Joshi-Imre, D. Arreaga-Salas, G. Gutierrez-Heredia, A. C. Duran-Martinez and J. Nathan, *Journal of Neural engineering* **2018**, *15*, 045002.
- [95] M. Gonzalez, F. Axisa, M. V. Bulcke, D. Brosteaux, B. Vandeveldel and J. Vanfleteren, *Microelectronics Reliability* **2008**, *48*, 825-832.

- [96] Y. Sun, W. M. Choi, H. Jiang, Y. Y. Huang and J. A. Rogers, *Nature Nanotechnology* **2006**, *1*, 201-207.
- [97] J. Liang, K. Tong and Q. Pei, *Advanced Materials* **2016**, *28*, 5986-5996.
- [98] R. R. Bourne, S. R. Flaxman, T. Braithwaite, M. V. Cicinelli, A. Das, J. B. Jonas, J. Keeffe, J. H. Kempen, J. Leasher and H. Limburg, *The Lancet Global Health* **2017**, *5*, e888-e897.
- [99] J. Kim, B.-K. Han, D. Pyo, S. Ryu, H. Kim and D.-S. Kwon, *IEEE Transactions on Haptics* **2020**, *13*, 59-65.
- [100] B. Mosadegh, A. D. Mazzeo, R. F. Shepherd, S. A. Morin, U. Gupta, I. Z. Sani, D. Lai, S. Takayama and G. M. Whitesides, *Lab on a Chip* **2014**, *14*, 189-199.
- [101] H.-C. Cho, B.-S. Kim, J.-J. Park and J.-B. Song, *2006 SICE-ICASE International Joint Conference* **2006**, pp. 1917-1921.
- [102] R. Velázquez, H. Hernández and E. Preza, *Applied Bionics and Biomechanics* **2012**, *9*, 45-60.
- [103] D. Leonardis, L. Claudio and A. Frisoli, *International Conference on Applied Human Factors and Ergonomics* **2017**, pp. 488-498.
- [104] G. C. Bettelani, G. Averta, M. G. Catalano, B. Leporini and M. Bianchi, *IEEE Transactions on Haptics* **2020**, *13*, 239-245.
- [105] M. E. Adnan, N. M. Dastagir, J. Jabin, A. M. Chowdhury and M. R. Islam, *2017 IEEE Region 10 Humanitarian Technology Conference (R10-HTC)* **2017**, pp. 175-178.
- [106] Y. Qiu, Z. Lu and Q. Pei, *ACS applied Materials & Interfaces* **2018**, *10*, 24807-24815.
- [107] N. H. Runyan and F. Carpi, *Expert Review of Medical Devices* **2011**, *8*, 529-532.